SIAM J. Imaging Sciences
Vol. 11, No. 4, pp. 2786–2814

Analyzing Reconstruction Artifacts from Arbitrary Incomplete X-ray CT Data*

Leise Borg†, Jürgen Frikel‡, Jakob Sauer Jørgensen§, and Eric Todd Quinto¶

Abstract. This article provides a mathematical analysis of singular (nonsmooth) artifacts added to reconstructions by filtered backprojection (FBP) type algorithms for X-ray computed tomography (CT) with arbitrary incomplete data. We prove that these singular artifacts arise from points at the boundary of the data set. Our results show that, depending on the geometry of this boundary, two types of artifacts can arise: object-dependent and object-independent artifacts. Object-dependent artifacts are generated by singularities of the object being scanned, and these artifacts can extend along lines. They generalize the streak artifacts observed in limited-angle tomography. Object-independent artifacts, on the other hand, are essentially independent of the object and take one of two forms: streaks on lines if the boundary of the data set is not smooth at a point and curved artifacts if the boundary is smooth locally. We prove that these streak and curve artifacts are the only singular artifacts that can occur for FBP in the continuous case. In addition to the geometric description of artifacts, the article provides characterizations of their strength in Sobolev scale in certain cases. The results of this article apply to the well-known incomplete data problems, including limited-angle and region-of-interest tomography, as well as to unconventional X-ray CT imaging setups that arise in new practical applications. Reconstructions from simulated and real data are analyzed to illustrate our theorems, including the reconstruction that motivated this work—a synchrotron data set in which artifacts appear on lines that have no relation to the object.

Key words. X-ray tomography, incomplete data tomography, limited-angle tomography, region-of-interest tomography, reconstruction artifact, wavefront set, microlocal analysis, Fourier integral operators

AMS subject classifications. 44A12, 92C55, 35S30, 58J40

DOI. 10.1137/18M1166833

1. Introduction.

Over the past decades, computed tomography (CT) has established itself as a standard imaging technique in many areas, including materials science and medical imaging. One collects X-ray measurements from many different directions (lines) that are dis-

*Received by the editors January 24, 2018; accepted for publication (in revised form) September 28, 2018; published electronically December 6, 2018. The original version of this article appeared online as https://arxiv.org/abs/1707.03055.

http://www.siam.org/journals/siims/11-4/M116683.html

Funding: The first author's research was partially supported by Innovation Fund Denmark and Maersk Oil and Gas. The second author's research was partially supported by the HC Ørsted Postdoc programme, co-funded by Marie Curie Actions at the Technical University of Denmark. The third author's research was partially supported by ERC Advanced grant 291405 and EPSRC grant EP/P02226X/1. The fourth author's research was partially supported by the Otto Mønsteds Fond, the Tufts FRAC, and NSF grants DMS 1311558 and DMS 1712207.

†Department of Computer Science, University of Copenhagen, Copenhagen 2100, Denmark (lebo@di.ku.dk).

‡Department of Computer Science and Mathematics, OTH Regensburg, Regensburg 93053, Germany (juergen.frikel@oth-regensburg.de).

§School of Mathematics, University of Manchester, Manchester M13 9PL, UK (jakob.jorgensen@manchester.ac.uk).

¶Department of Mathematics, Tufts University, Medford, MA 02155 (todd.quinto@tufts.edu, http://math.tufts.edu/faculty/equinto/).

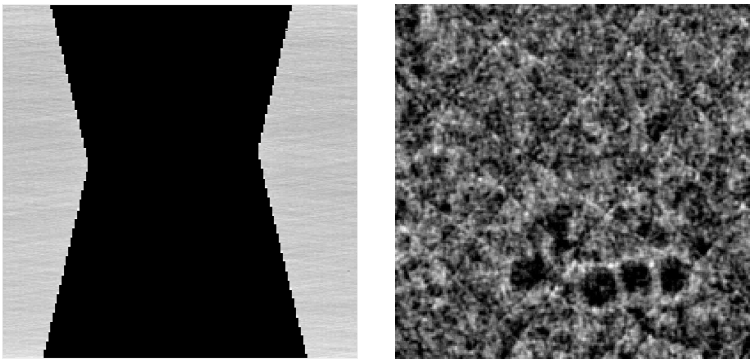

Figure 1. *Left: A small part of the sinogram of the chalk sample analyzed in section 7. Notice that the boundary of the data set in this enlargement is jagged. Right: Small central section of a reconstruction of the chalk. Notice the streak artifacts over lines in the reconstruction. Monochromatic parallel beam data were taken of the entire cross section of the chalk over* 1,800 *views covering* 180 *degrees, and there were* 2,048 × 2,048 *detector elements with a* 0.5 *mm field of view, providing micrometer resolution of the sample. Data* [59] *obtained, with thanks to the Japan Synchrotron Radiation Research Institute from beam time on beamline BL*20*XU of SPring-*8 *(Proposal* 2015*A*1147*). For more details, see section* 7 *and* [6,]

tributed all around the object. Then, one reconstructs a picture of the interior of the object using an appropriate mathematical algorithm. In classical tomographic imaging setups, this procedure works very well because the data can be collected all around the object, i.e., the data are *complete*, and standard reconstruction algorithms, such as filtered backprojection (FBP), provide accurate reconstructions [34, 43]. However, in many CT problems, some data are not available, and this leads to incomplete (or limited) data sets. The reasons for data incompleteness might be patient related (e.g., to decrease dose) or practical (e.g., when the scanner cannot image all of the object, as in digital breast tomosynthesis).

Classical incomplete data problems have been studied from the beginning of tomography, including *limited-angle tomography*, where the data can be collected only from certain view-angles [25, 31]; *interior* or *region-of-interest (ROI) tomography*, where the X-ray measurements are available only over lines intersecting a subregion of the object [13, 26, 51]; and *exterior tomography*, where measurements are available only over all lines outside a subregion [33, 48].

In addition, new scanning methods generate novel data sets, such as the synchrotron experiment [6, 7] in section 7 that motivated this research. That reconstruction, in Figure 1, includes dramatic streaks that are independent of the object and were not described in the mathematical theory at that time but are explained by our main theorems. A thorough practical investigation of this particular problem was recently presented in [6].

Regardless of the type of data incompleteness, in most practical CT problems a variant of FBP is used on the incomplete data to produce reconstructions [43]. It is well known that incomplete data reconstruction problems that do not incorporate a priori information (as is the case in all FBP type reconstructions) are severely ill-posed (see, e.g., [32] or [35, section 6] for limited-angle CT). Consequently, certain image features cannot be reconstructed reliably [47], and, in general, artifacts such as the limited-angle streaks in Figure 2 in section 4 can occur. Therefore, reconstruction quality suffers considerably, and this complicates the

proper interpretation of images.

We consider the continuous case, so that we do not evaluate discretization errors. By *artifacts* we mean nonsmooth image features (singularities), such as streaks, that are added to the reconstruction by the algorithm and are not part of the original object (see Definition 3.3).

1.1. Related research in the mathematical literature. Our work is based on microlocal analysis, a deep theory that describes how singularities are transformed by Fourier integral operators (FIOs), such as the X-ray transform. Early articles using microlocal analysis in tomography include [41], which considers nonlinear artifacts in X-ray CT; [47], which characterizes visible and invisible singularities from X-ray CT data; [19], which provided a general microlocal framework for admissible complexes; and [29], which considers general measures on lines in $\mathbb{R}^2$. Subsequently, artifacts were extensively studied in the context of limited-angle tomography in, e.g., [25] and then [16]. The strength of added artifacts in limited-angle tomography was analyzed in [36]. Similar characterizations of artifacts in limited-angle type reconstructions have also been derived for the generalized Radon line and hyperplane transforms as well as for other Radon transforms (such as circular and spherical Radon transforms); see [1, 17, 18, 37, 38].

Metal in objects can corrupt CT data and create dramatic streak artifacts [4]. This can be dealt with as an incomplete data problem by excluding data over lines through the metal. Recently, this problem has been mathematically modeled in a sophisticated way using microlocal analysis in [40, 44, 52]. A related problem is studied in [9, 39, 42], where the authors develop a streak reduction method for quantitative susceptibility mapping. Moreover, microlocal analysis has been used to analyze properties of related integral transforms in pure and applied settings [5, 14, 19, 50, 55].

1.2. Basic mathematical setup and our results. We use microlocal analysis to present a unified approach for analyzing reconstruction artifacts for arbitrary incomplete X-ray CT data that are caused by the choice of data set. We not only consider all of the above mentioned classical incomplete data problems but also emerging imaging situations with incomplete data. We provide a geometric characterization of the artifacts, and we prove that it describes all singular artifacts that can occur for FBP type algorithms in the continuous case.

If f is the density of the object to be reconstructed, then each CT measurement is modeled by a line integral of f over a line in the data set. As we will describe in section 2.1, we parameterize lines by $(\theta, p) \in S^1 \times \mathbb{R}$, and the CT measurement of f over the line $L(\theta, p)$ is denoted by $Rf(\theta, p)$. With complete data, where $Rf(\theta, p)$ is given over all $(\theta, p) \in S^1 \times \mathbb{R}$, accurate reconstructions can be produced by the FBP algorithm. In incomplete data CT problems, the data are taken over lines $L(\theta, p)$ for (θ, p) in a proper subset, A, of $S^1 \times \mathbb{R}$, and, even though FBP is designed for complete data, it is still one of the preferred reconstruction methods in practice; see [43]. As a result, incomplete data CT reconstructions usually suffer from artifacts.

We prove that incomplete data artifacts arise from points at the boundary or "edge" of the data set, $\mathrm{bd}(A)$, and we show that there are two types of artifacts: *object-dependent* and *object-independent* artifacts. The object-dependent artifacts are caused by singularities of the object being scanned. In this case, artifacts can appear all along a line $L(\theta_0, p_0)$ (i.e., a streak)

if $(\theta_0, p_0) \in \mathrm{bd}(A)$ *and* if there is a singularity of the object on the line (such as a jump or object boundary tangent to the line)—this singularity of the object "generates" the artifact (see Theorem 3.7A.). The streak artifacts observed in limited-angle tomography are special cases of this type of artifact.

The object-independent artifacts are essentially independent of the object being scanned (they depend primarily on the geometry of $\mathrm{bd}(A)$), and they can appear either on lines or on curves. If the boundary of A is smooth near a point $(\theta_0, p_0) \in \mathrm{bd}(A)$, then we prove that artifacts can appear in the reconstruction along curves generated by $\mathrm{bd}(A)$ near (θ_0, p_0), and they can occur whether the object being scanned has singularities or not (see Theorem 3.5B(3). We also prove that if $\mathrm{bd}(A)$ is not smooth (see Definition 3.2) at a point (θ_0, p_0), then, essentially independently of the object, an artifact line can be generated all along $L(\theta_0, p_0)$ (see Theorem 3.7C.).

We will illustrate our results with reconstructions for classical problems including limited-angle tomography and ROI tomography, as well as problems with novel data sets, including the synchrotron data set in Figure 1. In addition, we provide estimates of the strength of the artifacts in Sobolev scale.

To the best of our knowledge, the mathematical literature up until now used microlocal and functional analysis to explain streak artifacts on lines that are generated by singularities of the object, *and* they exclusively focused on specific problems, primarily limited-angle tomography (see, e.g., [16, 25, 36]). Important work was done to analyze visible singularities for ROI (or local) tomography (see, e.g., [13, 26, 29, 47, 51]). However, we are not aware of any reference where a microlocal explanation for the ring artifact in ROI CT was provided, although researchers are well aware of the ring itself (see, e.g., [8, 11]). We are also not aware of microlocal analyses of more general imaging setups, such as the nonstandard one presented in Figure 1.

1.3. Organization of the article. In section 2, we provide notation and some of the basic ideas about wavefront sets. In section 3, we give our main theoretical results, and in section 4, we apply them to explain added artifacts in reconstructions from classical and novel limited data sets. In section 5, we describe the strength of added artifacts in Sobolev scale. Then, in section 6, we describe a simple, known method to decrease the added artifacts and provide a reconstruction and theorem to justify the method. We provide more details of the synchrotron experiment in section 7 and observations and generalizations in section 8. Finally, in Appendix A, we give some technical theorems and then prove the main theorems.

2. Mathematical basis. Much of our theory can be made rigorous for distributions of compact support (see [15, 53] for an overview of distributions), but we will consider only Lebesgue measurable functions. This setup is realistic in practice, and our theorems are simpler in this case than for general distributions. Remark A.4 provides perspective on this.

The set $L^2(D)$ is the set of square-integrable functions on the closed unit disk $D = \{x \in \mathbb{R}^2 : \|x\| \leq 1\}$. The set $L^2_{\mathrm{loc}}(\mathbb{R}^2)$ is the set of locally square-integrable functions—functions that are square-integrable over every compact subset of $\mathbb{R}^2$. We define $L^2_{\mathrm{loc}}(S^1 \times \mathbb{R})$ in a similar way, where S^1 is the circle of unit vectors in $\mathbb{R}^2$.

2.1. Notation. Let $(\theta, p) \in S^1 \times \mathbb{R}$; then the line perpendicular to θ and containing $p\theta$ is denoted by

$$L(\theta, p) = \left\{ x \in \mathbb{R}^2 : x \cdot \theta = p \right\}. \tag{2.1}$$

Note that $L(\theta, p) = L(-\theta, -p)$. For $\theta \in S^1$, let $\theta^\perp$ be the unit vector $\pi/2$ radians counterclockwise from θ. We define the *X-ray transform* or *Radon line transform* of $f \in L^2(D)$ to be the integral of f over $L(\theta, p)$:

$$Rf(\theta, p) = \int_{-\infty}^{\infty} f(p\theta + t\theta^\perp)\, \mathrm{d}t. \tag{2.2}$$

The symmetry of our parameterization of lines gives the symmetry condition

$$Rf(\theta, p) = Rf(-\theta, -p). \tag{2.3}$$

For functions g on $S^1 \times \mathbb{R}$, the *dual Radon transform* or *backprojection operator* is defined as

$$R^* g(x) = \int_{S^1} g(\theta, x \cdot \theta)\, \mathrm{d}\theta. \tag{2.4}$$

When visualizing functions on $S^1 \times \mathbb{R}$, we will use the natural identification

$$\mathbb{R}^2 \ni (\varphi, p) \mapsto (\overline{\theta}(\varphi), p) \in S^1 \times \mathbb{R}, \quad \text{where } \overline{\theta}(\varphi) := (\cos(\varphi), \sin(\varphi)) \in S^1, \tag{2.5}$$

and for functions g on $S^1 \times \mathbb{R}$ the identification

$$\widetilde{g}(\varphi, p) = g(\overline{\theta}(\varphi), p) \quad \text{for } (\varphi, p) \in \mathbb{R}^2. \tag{2.6}$$

The *sinogram* of a function $g(\theta, p)$ is a grayscale picture on $[0, \pi] \times \mathbb{R}$ or $[0, 2\pi] \times \mathbb{R}$ of the mapping $(\varphi, p) \mapsto \widetilde{g}(\varphi, p)$.

2.2. Wavefront sets. In this section, we define some important concepts needed to describe singularities in general. Sources, such as [15], provide introductions to microlocal analysis. Generally cotangent spaces are used to describe microlocal ideas, but they would complicate this exposition, so we will identify a covector $(x, \xi \mathrm{dx})$ with the associated ordered pair of vectors (x, ξ). The book chapter [27] provides some basic microlocal ideas and a more elementary exposition adapted for tomography.

The concept of the wavefront set is a central notion of microlocal analysis. It defines singularities of functions in a way that simultaneously provides information about their location and direction. We will employ this concept to define (singular) artifacts precisely, and we will use the powerful theory of microlocal analysis to analyze artifacts generated in incomplete data reconstructions in tomography.

In what follows, by a *cutoff function at* $x_0 \in \mathbb{R}^2$ we will denote a C^∞-function of compact support that is nonzero at x_0. We now define singularities and the wavefront set.

Definition 2.1 (wavefront set [15, 56]). *Let $x_0 \in \mathbb{R}^2$, $\xi_0 \in \mathbb{R}^2 \setminus \mathbf{0}$, and $f \in L^2_{loc}(\mathbb{R}^2)$. We say f is* smooth at x_0 in direction ξ_0 *if there are a cutoff function ψ at x_0 and an open cone V containing ξ_0 such that the Fourier transform $\mathcal{F}(\psi f)(\xi)$ is rapidly decaying at infinity for $\xi \in V$.*[1]

We say f has a singularity at x_0 in direction ξ_0*, or a singularity at (x_0, ξ_0), if f is not smooth at x_0 in direction ξ_0. We say that f has a* singularity *at x_0 if f is not smooth at x_0 in some direction.*

The wavefront set of f, $\mathrm{WF}(f)$, *is defined as the set of all singularities (x_0, ξ_0) of f.*

For $(x_0, \xi_0) \in \mathrm{WF}(f)$, the first entry x_0 will be called the *base point* of (x_0, ξ_0). Hence, the base point of a singularity gives the location where the function f is singular (not smooth) in some direction. If we say f has a singularity at x_0, we mean x_0 is the base point of an element of $\mathrm{WF}(f)$.

As an example, let B be a subset of the plane with a smooth boundary and let f be equal to 1 on B and 0 off of B. Then, $\mathrm{WF}(f)$ is the set of all points (x, ξ) where the base points x are on the boundary of B and ξ is normal to the boundary of B at x. In this case, f has singularities at all points of $\mathrm{bd}(B)$.

Remark 2.2 (wavefront set for functions defined on $S^1 \times \mathbb{R}$). The notion of a singularity and the wavefront set can also be defined for functions $g \in L^2_{\mathrm{loc}}(S^1 \times \mathbb{R})$ using the identification (2.6).

In order to define $\mathrm{WF}(g)$, let $\widetilde{g}$ denote the locally square-integrable function on $\mathbb{R}^2$ defined by (2.6). Let $(\theta, p) \in S^1 \times \mathbb{R}$ and $\varphi \in \mathbb{R}$ with $\theta = \overline{\theta}(\varphi)$. Let $\eta \in \mathbb{R}^2 \setminus \mathbf{0}$. Then, we say that g has a singularity at $((\theta, p), \eta)$ if $\widetilde{g}$ has a singularity at $((\varphi, p), \eta)$, i.e., $((\theta, p), \eta) \in \mathrm{WF}(g)$ if $((\varphi, p), \eta) \in \mathrm{WF}(\widetilde{g})$. In that case, the base point of a singularity of g is of the form (θ, p).

Note that the wavefront set is well-defined for functions on $S^1 \times \mathbb{R}$ as both $\widetilde{g}$ and $\varphi \mapsto \overline{\theta}(\varphi)$ are 2π-periodic in φ.

Definition 2.3. *Let $(\theta, p) \in S^1 \times \mathbb{R}$. The* normal space of the line $L(\theta, p)$ *is*

$$N(L(\theta, p)) = \{(x, \omega\theta) : x \in L(\theta, p), \omega \in \mathbb{R}\}. \tag{2.7}$$

For $f \in L^2_{loc}(\mathbb{R}^2)$, the set of singularities of f normal to $L(\theta, p)$ is

$$\mathrm{WF}_{L(\theta,p)}(f) = \mathrm{WF}(f) \cap N(L(\theta, p)). \tag{2.8}$$

If $\mathrm{WF}_{L(\theta,p)}(f) \neq \emptyset$, then we say f has a singularity (or singularities) normal to $L(\theta, p)$.
If $\mathrm{WF}_{L(\theta,p)}(f) = \emptyset$, then we say f is smooth normal to the line $L(\theta, p)$.
For $x_0 \in \mathbb{R}^2$, we let

$$\mathrm{WF}_{x_0}(f) = \mathrm{WF}(f) \cap \left(\{x_0\} \times \mathbb{R}^2\right).$$

For $g \in L^2_{loc}(S^1 \times \mathbb{R})$, we define

$$\mathrm{WF}_{(\theta,p)}(g) = \mathrm{WF}(g) \cap \left(\{(\theta, p)\} \times \mathbb{R}^2\right). \tag{2.9}$$

[1] That is, for every $k \in \mathbb{N}$, there is a constant $C_k > 0$ such that $|\mathcal{F}(\psi f)(\xi)| \leq C_k/(1 + \|\xi\|)^k$ for all $\xi \in V$.

It is important to understand each set introduced in Definition 2.3: $N(L(\theta,p))$ is the set of all (x,ξ) such that $x \in L(\theta,p)$, and the vector ξ is normal to $L(\theta,p)$ at x. Therefore, $\mathrm{WF}_{L(\theta,p)}(f)$ is the set of wavefront directions $(x,\xi) \in \mathrm{WF}(f)$ with $x \in L(\theta,p)$ and ξ normal to this line.

The set $\mathrm{WF}_{x_0}(f)$ is the wavefront set of f above x_0, and $\mathrm{WF}_{x_0}(f) = \emptyset$ if and only if f is smooth in some neighborhood of x_0 [15].

If $g \in L^2_{\mathrm{loc}}(S^1 \times \mathbb{R})$, then $\mathrm{WF}_{(\theta,p)}(g)$ is the set of wavefront directions with base point (θ,p). We will exploit the sets introduced in these definitions starting in the next section.

3. Main results.

In contrast to limited-angle characterizations in [16, 25], our main results describe artifacts in arbitrary incomplete data reconstructions that include the classical limited data problems as special cases. Our results are formulated in terms of the wavefront set (Definition 2.1), which provides a precise concept of singularity.

In many applications, reconstructions from incomplete CT data are calculated by the filtered backprojection (FBP) algorithm, which is designed for complete data (see [43] for a practical discussion of FBP). In this case, the incomplete data are often extended by the algorithm to a complete data set on $S^1 \times \mathbb{R}$ by setting it to zero off of the set A (*cutoff region*) over which data are taken. Therefore, the incomplete CT data can be modeled as

$$R_A f(\theta,p) = \mathbb{1}_A(\theta,p) Rf(\theta,p), \tag{3.1}$$

where $\mathbb{1}_A$ is the characteristic function of A.[2] Thus, using the FBP algorithm to calculate a reconstruction from such data gives rise to the reconstruction operator

$$\mathcal{L}_A f = R^* (\Lambda R_A f) = R^* (\Lambda \mathbb{1}_A Rf), \tag{3.2}$$

where Λ is the standard FBP filter (see, e.g., [34, Theorem 2.5] and [35, section 5.1.1] for numerical implementations) and R^* is defined by (2.4).

Our next assumption collects the conditions we will impose on the cutoff region A. There, we will use the notation $\mathrm{int}(A)$, $\mathrm{bd}(A)$, and $\mathrm{ext}(A)$ to denote the interior of A, the boundary of A, and the exterior of A, respectively.

Assumption 3.1. Let A be a proper subset of $S^1 \times \mathbb{R}$ (i.e., $A \neq S^1 \times \mathbb{R}$) with a nontrivial interior, and assume A is symmetric in the following sense:

$$\text{if } (\theta,p) \in A, \text{ then } (-\theta,-p) \in A. \tag{3.3}$$

In addition, assume that A is the smallest closed set containing $\mathrm{int}(A)$, i.e., $A = \mathrm{cl}(\mathrm{int}(A))$.

We now explain the importance of this assumption. Since A is proper, data over A are incomplete. Being symmetric means that if $(\theta,p) \in A$, then the other parameterization of $L(\theta,p)$ is also in A. We exclude degenerate cases, such as when A includes an isolated curve by assuming that $A = \mathrm{cl}(\mathrm{int}(A))$.

Our next definition gives us the language to describe the geometry of $\mathrm{bd}(A)$.

[2] The characteristic function of a set A is the function that is equal to one on A and zero outside of A.

Definition 3.2 (smoothness of $\mathrm{bd}(A)$). *Let $A \subset S^1 \times \mathbb{R}$, and let $(\theta_0, p_0) \in \mathrm{bd}(A)$.*

- *We say that* $\mathrm{bd}(A)$ *is* smooth near (θ_0, p_0) *if, for some neighborhood U of (θ_0, p_0) in $S^1 \times \mathbb{R}$, the part of* $\mathrm{bd}(A)$ *in U is a C^∞ curve. In this case, there is a unique tangent line in (θ, p)-space to* $\mathrm{bd}(A)$ *at (θ_0, p_0).*
  - *If this tangent line is vertical (i.e., of the form $\theta = \theta_0$), then we say the boundary* is vertical *or* has infinite slope *at (θ_0, p_0).*
  - *If this tangent line is not vertical, then* $\mathrm{bd}(A)$ *is defined near (θ_0, p_0) by a smooth function $p = p(\theta)$. In this case, the* slope of the boundary at (θ_0, p_0) *will be the slope of this tangent line:*

$$p'(\theta_0) := \frac{dp}{d\varphi}\left(\overline{\theta}(\varphi_0)\right), \quad \text{where } \varphi_0 \text{ is defined by } \overline{\theta}(\varphi_0) = \theta_0. \tag{3.4}$$

[3]

- *We say that* $\mathrm{bd}(A)$ *is* not smooth at (θ_0, p_0) *if it is not a smooth curve in any neighborhood of (θ_0, p_0).*
  - *We say that* $\mathrm{bd}(A)$ *has* a corner at (θ_0, p_0) *if the curve* $\mathrm{bd}(A)$ *is continuous at (θ_0, p_0), is smooth at all other points sufficiently close to (θ_0, p_0), and has two different one-sided tangent lines at (θ_0, p_0).*[4]

3.1. Singularities and artifacts. In this section, we define artifacts and visible and invisible singularities, and we explain why artifacts appear on lines $L(\theta, p)$ only when $(\theta, p) \in \mathrm{bd}(A)$.

Definition 3.3 (artifacts and visible singularities). *Every singularity $(x, \xi) \in \mathrm{WF}(\mathcal{L}_A f)$ that is not a singularity of f is called an* artifact *(i.e., any singularity in $\mathrm{WF}(\mathcal{L}_A f) \setminus \mathrm{WF}(f)$).*

An artifact curve *is a collection of base points of artifacts that form a curve.*

A streak artifact *is an artifact curve in which the curve is a subset of a line.*

Every singularity of f that is also in $\mathrm{WF}(\mathcal{L}_A f)$ is said to be visible *(from data on A), i.e., any singularity in $\mathrm{WF}(\mathcal{L}_A f) \cap \mathrm{WF}(f)$. Other singularities of f are called* invisible *(from data on A).*[5]

Our next theorem gives an analysis of singularities in $\mathcal{L}_A f$ corresponding to lines $L(\theta, p)$ for $(\theta, p) \notin \mathrm{bd}(A)$. It shows that the only singularities of $\mathcal{L}_A f$ that are normal to lines $L(\theta, p)$ for $(\theta, p) \in \mathrm{int}(A)$ are visible singularities of f, and there are no singularities of $\mathcal{L}_A f$ normal to lines $L(\theta, p)$ for $(\theta, p) \in \mathrm{ext}(A)$.

Theorem 3.4 (visible and invisible singularities in the reconstruction). *Let $f \in L^2(D)$, and let $A \subset S^1 \times \mathbb{R}$ satisfy Assumption 3.1.*

A. *If $(\theta, p) \in \mathrm{int}(A)$, then $\mathrm{WF}_{L(\theta,p)}(f) = \mathrm{WF}_{L(\theta,p)}(\mathcal{L}_A f)$. Therefore, all singularities of f normal to $L(\theta, p)$ are visible singularities, and $\mathcal{L}_A f$ has no artifacts normal to $L(\theta, p)$.*

[3] Note that the map $\varphi \mapsto \overline{\theta}(\varphi)$ gives the local coordinates on S^1 near φ_0 and θ_0 that are used in our proofs, and p' is just the derivative of p in these coordinates.

[4] Precisely, there is an open neighborhood U of (θ_0, p_0), an open interval $I = (a, b)$, two smooth functions $c_i : I \to U$, $i = 1, 2$, and some $t_0 \in I$ such that $c_i(t_0) = (\theta_0, p_0)$, $i = 1, 2$; the curves $c_1(I)$ and $c_2(I)$ intersect transversally at (θ_0, p_0); and $\mathrm{bd}(A) \cap U = c_1((a, t_0]) \cup c_2((a, t_0])$.

[5] Invisible singularities of f are smoothed by $\mathcal{L}_A$, and the reconstruction of those singularities is in general extremely ill-posed in Sobolev scale since any inverse operator must take each smoothed singularity back to the original nonsmooth singularity, so inversion would be discontinuous in any range of Sobolev norms.

B. *If* $(\theta,p)\notin(A\cap\operatorname{supp}(Rf))$, *then* $\mathrm{WF}_{L(\theta,p)}(\mathcal{L}_A f)=\emptyset$. *Therefore, all singularities of* f *normal to* $L(\theta,p)$ *are invisible from data on* A, *and* $\mathcal{L}_A f$ *has no artifacts normal to* $L(\theta,p)$.

C. *If* $x\in D$ *and all lines through* x *are parameterized by points in* $\operatorname{int}(A)$ *(i.e., for all* $\theta\in S^1$, $(\theta,x\cdot\theta)\in\operatorname{int}(A)$*), then*

$$\mathrm{WF}_x(f)=\mathrm{WF}_x(\mathcal{L}_A f). \tag{3.5}$$

In this case, all singularities of f *at* x *are visible in* $\mathcal{L}_A f$.

Therefore, artifacts occur only normal to lines $L(\theta,p)$ *for* $(\theta,p)\in\operatorname{bd}(A)$.

This theorem follows directly from [47, Theorem 3.1] and the continuity of R^* (see also [29]). Note that Theorem 3.4C. follows from parts 3.4A. and 3.4B. and is included because we will need it later.

3.2. Analyzing singular artifacts. We now analyze artifacts in limited data FBP reconstructions using $\mathcal{L}_A$ (3.2). In particular, we show that the nature of artifacts depends on the smoothness and geometry of $\operatorname{bd}(A)$ and, in some cases, singularities of the object f.

Theorem 3.4 establishes that artifacts occur only above points on lines $L(\theta,p)$ for $(\theta,p)\in\operatorname{bd}(A)$. Our next two theorems show that the only artifacts that occur are either artifacts on specific types of curves (see (3.6)) or streak artifacts, and they are of two types.

Let $f\in L^2(D)$, and let $(\theta,p)\in\operatorname{bd}(A)$:

- **Object-independent artifacts:** These are caused essentially by the geometry of $\operatorname{bd}(A)$. They can occur whether f has singularities normal to $L(\theta,p)$ or not, and they can be curves or streak artifacts.
- **Object-dependent artifacts:** These are caused essentially by singularities of the object f that are normal to $L(\theta,p)$. They will not occur if f is smooth normal to $L(\theta,p)$, and they are always streak artifacts.

Our next theorem gives conditions under which artifact curves that are not streaks (i.e., not subsets of lines) appear in reconstructions from $\mathcal{L}_A$.

Theorem 3.5 (artifact curves). *Let* $f\in L^2(D)$, *and let* $A\subset S^1\times\mathbb{R}$ *satisfy Assumption* 3.1. *Let* $(\theta_0,p_0)\in\operatorname{bd}(A)$, *and assume that* $\operatorname{bd}(A)$ *is smooth near* (θ_0,p_0). *Assume* $\operatorname{bd}(A)$ *has finite slope at* (θ_0,p_0), *and let* I *be a neighborhood of* θ_0 *in* S^1 *such that* $\operatorname{bd}(A)$ *is given by a smooth curve* $p=p(\theta)$ *near* (θ_0,p_0). *Let*

$$x_b=x_b(\theta)=p(\theta)\theta+p'(\theta)\theta^{\perp}\in\mathbb{R}^2 \quad \text{for } \theta\in I. \tag{3.6}$$

Then, an object-independent artifact curve can appear in $\mathcal{L}_A f$ *on the curve given by* $I\ni\theta\mapsto x_b(\theta)$, *which we will call the* x_b-curve*:*

A. *The* x_b*-curve is curved (i.e., not a subset of a line) unless it is a point.*

B. *Assume* f *is smooth normal to* $L(\theta_0,p_0)$.

(1) *Then,*

$$\mathrm{WF}_{L(\theta_0,p_0)}(\mathcal{L}_A f)\subset\{(x_b(\theta_0),\omega\theta_0):\omega\neq 0\}. \tag{3.7}$$

(2) *If* $Rf=0$ *in a neighborhood of* (θ_0,p_0), *then* $\mathrm{WF}_{L(\theta_0,p_0)}(\mathcal{L}_A f)=\emptyset$ *and this* x_b*-curve will not appear in the reconstruction* $\mathcal{L}_A f$ *near* $x_b(\theta_0)$.

(3) *If* $Rf(\theta_0, p_0) \neq 0$*, then equality holds in* (3.7) *and the* x_b*-curve will appear in the reconstruction* $\mathcal{L}_A f$ *near* $x_b(\theta_0)$*.*

Theorem 3.5 is proved in Appendix A.2. Figures 3, 4, and 5 in section 4 all show x_b-artifact curves. The following remark discusses these curves in more detail.

Remark 3.6. Assume $\mathrm{bd}(A)$ is smooth with finite slope at (θ_0, p_0). Let I be a neighborhood of θ_0, and let $p : I \to \mathbb{R}$ be a parameterization of $\mathrm{bd}(A)$ near (θ_0, p_0). Note that

$$x_b(\theta) \in L(\theta, p) \quad \text{for} \quad \theta \in I.$$

If the slope of $\mathrm{bd}(A)$ at (θ_0, p_0) is small enough, i.e.,

$$|p'(\theta_0)| < \sqrt{1 - p_0^2} \tag{3.8}$$

holds, then the x_b-curve of artifacts $\theta \mapsto x_b(\theta)$ will be inside the closed unit disk, D, at least for θ near θ_0. If not, then $x_b(\theta_0) \notin \mathrm{int}(D)$. This is illustrated in section 4 in Figure 3a for large slope, where (3.8) is not satisfied, and in Figure 3b for small slope, where (3.8) is satisfied.

If $\mathrm{bd}(A)$ is smooth and vertical at (θ_0, p_0) (infinite slope), then there will be no object-independent artifact on the line $L(\theta_0, p_0)$. This follows from the proof of this theorem because the singularity in the data that causes the x_b curve is smoothed by R^* in this case. Intuitively, if $\mathrm{bd}(A)$ is vertical, then $p'(\theta_0)$ is infinite, and from (3.6) the point $x_b(\theta_0)$ would be "at infinity." In this case, only object-dependent streak artifacts can be generated by (θ_0, p_0); see Theorem 3.7 and Figures 2 and 3 in section 4.

Our next theorem gives the conditions under which there can be streak artifacts in reconstructions using $\mathcal{L}_A$.

Theorem 3.7 (streak artifacts). *Let* $f \in L^2(D)$*, and let* $A \subset S^1 \times \mathbb{R}$ *satisfy Assumption* 3.1*:*

A. *If* f *has a singularity normal to* $L(\theta_0, p_0)$*, then a streak artifact can occur on* $L(\theta_0, p_0)$*.*

B. *If* f *is smooth normal to* $L(\theta_0, p_0)$ *and* $\mathrm{bd}(A)$ *is smooth and vertical at* (θ_0, p_0)*, then* $\mathcal{L}_A f$ *is smooth normal to* $L(\theta_0, p_0)$*.*[6]

C. *Let* $(\theta_0, p_0) \in \mathrm{bd}(A)$*, and assume that* $\mathrm{bd}(A)$ *is not smooth at* (θ_0, p_0)*. Then,* $\mathcal{L}_A f$ *can have a streak artifact on* $L(\theta_0, p_0)$ *independent of* f*.*

If f *is smooth normal to* $L(\theta_0, p_0)$*, then* $Rf(\theta_0, p_0) \neq 0$*, and if* $\mathrm{bd}(A)$ *has a corner at* (θ_0, p_0) *(see Definition* 3.2*), then* $\mathcal{L}_A f$ does *have a streak artifact on* $L(\theta_0, p_0)$*, i.e.,*

$$\mathrm{WF}_{L(\theta_0, p_0)}(\mathcal{L}_A f) = N(L(\theta_0, p_0)).$$

The proof of Theorem 3.7 is provided in Appendix A.2.

Theorem 3.7A. provides a generalization of classical limited-angle streak artifacts observed in Figure 2 in section 4. Such limited-angle type artifacts can also be seen in Figures 3 and 5 in that section.

Theorem 3.7B. shows that the streak artifacts in part 3.7A. are object-dependent.

[6]Note that Theorem 3.5 B. states that if f is smooth normal to $L(\theta_0, p_0)$ and $\mathrm{bd}(A)$ is smooth and not vertical at (θ_0, p_0), then $\mathcal{L}_A f$ is smooth normal to $L(\theta_0, p_0)$ except possibly at $x_b(\theta_0)$ (see (3.7)).

Theorem 3.7C. explains the object-independent streak artifacts in Figure 5 that are highlighted in yellow as well as the object-independent streak artifacts that are observed in the real data reconstructions in Figure 9a in section 8. In Theorem 5.2, we will describe the strength of the artifacts in Sobolev scale in specific cases of Theorems 3.5 and 3.7.

Example 3.8. Theorems 3.5 and 3.7 give necessary conditions under which $\mathcal{L}_A f$ can have artifacts. We now provide an example when the conditions of those theorems hold for f and A but $\mathcal{L}_A f$ has no artifacts. This is why we state in parts of Theorems 3.5 and 3.7 that artifacts *can* occur rather than that they *will* occur.

Let $A = \{(\theta, p) \in S^1 \times \mathbb{R} : |p| \leq 1\}$; then A represents the set of lines meeting the closed unit disk, D. Let f be the characteristic function of D. Then, for all $x \in \mathrm{bd}(D) = S^1$, $\xi = (x, x) \in \mathrm{WF}(f)$, ξ is normal to the line $L(x, 1)$, and $(x, 1)$, which is in $S^1 \times \mathbb{R}$, is also in $\mathrm{bd}(A)$. Under these conditions, there *could* be a streak artifact on $L(x, 1)$ by Theorem 3.7A. Because $\mathrm{bd}(A)$ is smooth and not vertical, there *could* be an x_b-curve artifact by Theorem 3.5. However, $\mathbb{1}_A Rf = Rf$, so $\mathcal{L}_A f = f$ and there are no artifacts in this reconstruction.

Object-dependent streak artifacts were analyzed for limited-angle tomography in articles such as [16, 25, 36], but we are unaware of a reference to Theorem 3.7A. for general incomplete data problems. We are not aware of a previous reference in the literature to a microlocal analysis of the x_b-curve artifact as in Theorem 3.5 or to the corner artifacts as in Theorem 3.7C. We now assert that all singular artifacts are classified by Theorems 3.5 and 3.7.

Theorem 3.9. *Let $f \in L^2(D)$, and let $A \subset S^1 \times \mathbb{R}$ satisfy Assumption 3.1. The only singular artifacts in $\mathcal{L}_A f$ occur on x_b-curves as described by Theorem 3.5 or are streak artifacts as described by Theorem 3.7.*

Theorem 3.9 is proved in section A.2.

4. Numerical illustrations of our theoretical results.

We now consider a range of well-known incomplete data problems as well as unconventional ones to show how the theoretical results in section 3 are reflected in practice. All sinograms represent the data $g(\theta, p) = Rf(\theta, p)$ using (2.6) and displaying them in the (φ, p)-plane rather than showing them on $S^1 \times \mathbb{R}$. To this end, we define

$$
\begin{aligned}
&\widetilde{L}(\varphi, p) := L(\overline{\theta}(\varphi), p),\\
&(\varphi, p) \mapsto \widetilde{g}(\varphi, p) = g(\overline{\theta}(\varphi), p) \quad \text{for } \varphi \in [0, 2\pi],\ p \in [-\sqrt{2}, \sqrt{2}],\\
&\text{if } A \subset S^1 \times \mathbb{R}, \text{ then } \widetilde{A} := \{(\varphi, p) \in [0, 2\pi] \times \mathbb{R} : (\overline{\theta}(\varphi), p) \in A\}.
\end{aligned} \tag{4.1}
$$

In this section, we will specify limited data using the sets $\widetilde{A} \subset [0, 2\pi] \times \mathbb{R}$ rather than $A \subset S^1 \times \mathbb{R}$, and we will let R denote the Radon transform with this parameterization. Furthermore, because of the symmetry condition (2.3), we will display only the part of the sinogram in $[0, \pi] \times [-\sqrt{2}, \sqrt{2}]$. Except for the center picture in Figure 3a, reconstructions are displayed on $[-1, 1]^2$.

4.1. Limited-angle tomography.

First, we analyze limited-angle tomography, a classical problem in which Theorem 3.7A. applies. In this case, $\mathrm{bd}(\widetilde{A})$ consists of four vertical lines $\varphi = \varphi_1$, $\varphi = \varphi_2$, $\varphi = \varphi_1 + \pi$, $\varphi = \varphi_2 + \pi$ for two angles $0 \leq \varphi_1 < \varphi_2 < \pi$ representing the

ends of the angular range. Taking a closer look at the statement of Theorem 3.7A. and the results of [16, 18], one can observe that, locally, they describe the same phenomena; namely, whenever there is a line $\widetilde{L}(\varphi_0, p_0)$ in the data set with $(\varphi_0, p_0) \in \mathrm{bd}(\widetilde{A})$ and which is normal to a singularity of f, then a streak artifact can be generated on $\widetilde{L}(\varphi_0, p_0)$ in the reconstruction $\mathcal{L}_A f$. Therefore, Theorem 3.7A. generalizes the results of [16, 25] as it also applies to cutoff regions with a nonvertical tangent.

It is important to note that, with limited-angle data, there are no object-independent artifacts since $\mathrm{bd}(\widetilde{A})$ is smooth and vertical (the x_b-curve is not defined).

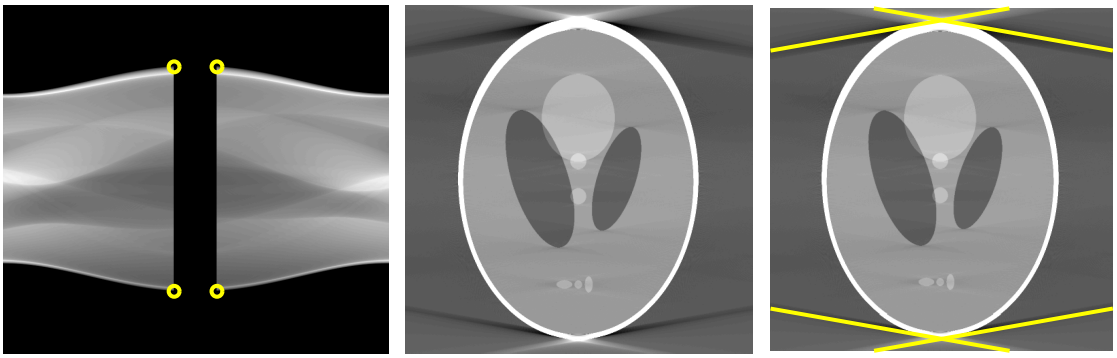

Figure 2. *Left: Limited-angle data (*$\mathrm{bd}(\widetilde{A})$ *is vertical). Center: FBP reconstruction. Right: Reconstruction highlighting object-dependent artifact lines tangent to the skull corresponding to the four circled points in the sinogram.*

Figure 2 illustrates limited-angle tomography. The boundary, $\mathrm{bd}(\widetilde{A})$, consists of the vertical lines $\varphi = 4\pi/9$ and $\varphi = 5\pi/9$. The artifact lines are exactly the lines with $\varphi = 4\pi/9$ or $5\pi/9$ that are tangent to boundaries in the object (i.e., wavefront directions are normal to the line). The four circled points on the sinogram correspond to the object-dependent artifact lines at the boundary of the skull. The corresponding lines are tangent to the skull and have angles $\varphi = 4\pi/9$ and $\varphi = 5\pi/9$. One can also observe artifact lines tangent to the inside of the skull with these same angles.

One can notice invisible singularities of f—the top and bottom boundaries of the skull—at the top and bottom of the reconstruction. If the excluded region in the sinogram were larger, the invisible singularities at the top and bottom of the object would be more noticeable.

4.2. Smooth boundary with finite slope. We now consider the general case in Theorem 3.5 by analyzing the artifacts for a specific set $\widetilde{A}$ which is defined as follows. It will be cut in the middle so that the leftmost boundary of A occurs at $\varphi = a := \frac{4}{9}\pi$; the rightmost boundary is constructed as $\varphi = b := \frac{5}{9}\pi$ for $p \le 0$ and

$$p(\varphi) = c\sqrt{\varphi - b}, \quad \varphi > b, \tag{4.2}$$

for $p > 0$ such that the two parts join differentiably at $(\varphi, p) = (0, 0)$. The steepness of the curved part of the rightmost boundary is governed by the constant c (as seen in the two sinograms in Figure 3).

According to the condition (3.8), the curved part of $\mathrm{bd}(\widetilde{A})$ is the only part that can potentially cause object-independent artifacts in D since the other parts are vertical. In

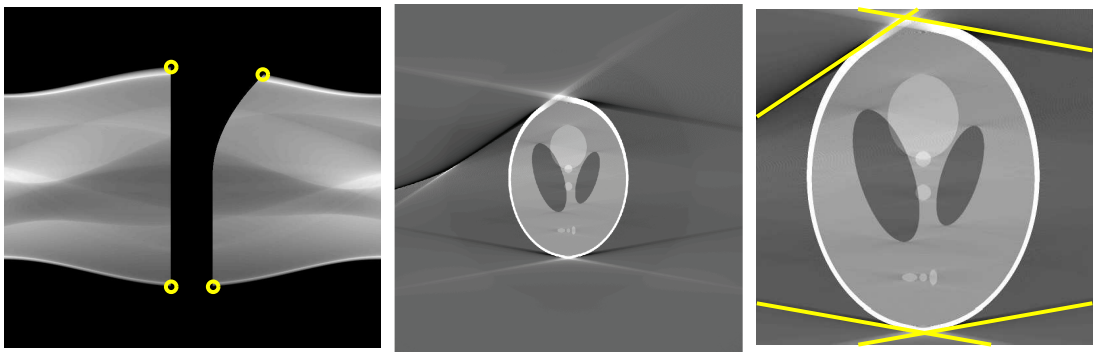

(a) Left: Sinogram with the boundary of $\widetilde{A}$ having large slope ($c = 1.3$). Center: FBP reconstruction over the larger region $[-2, 2]^2$ to show that the x_b-curve of artifacts is outside of the region displayed in the right frame. Right: Reconstruction highlighting object-dependent artifact lines tangent to the skull corresponding to the four circled points in the sinogram.

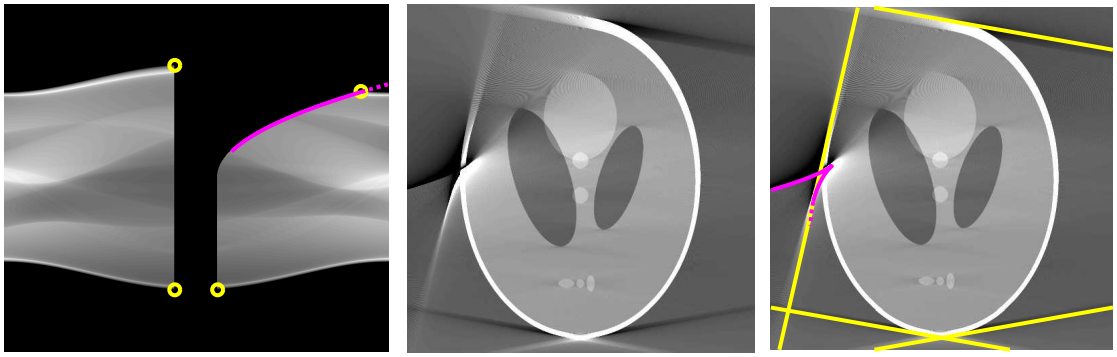

(b) Left: Sinogram with the boundary of $\widetilde{A}$ having small slope ($c = 0.65$). The part of the boundary causing the prominent x_b-curve of artifacts in the reconstruction region is highlighted in magenta. The solid part of the curve indicates the artifacts that are realized in the reconstruction. The dotted curve at the right end of the sinogram indicates potential artifacts that are not realized because the corresponding part of $\mathrm{bd}(\widetilde{A})$ is outside $\mathrm{supp}(Rf)$ (see Theorem 3.4B.). Center: FBP reconstruction. Right: Same FBP reconstruction as in the center image highlighting some of the added artifacts. The magenta curve in the reconstruction is the x_b-curve of artifacts, and the yellow artifact lines are object-dependent artifacts similar to those in Figure 3a.

Figure 3. *Illustration of artifacts for data sets with a smooth boundary given by (4.2). The x_b-curve $\varphi \mapsto x_b\left(\overline{\theta}(\varphi)\right)$ of artifacts is outside the reconstruction region in the top figure, and it meets the object in the bottom picture.*

Figure 3, we consider two data sets $\widetilde{A}$ with a smooth boundary: in Figure 3a, the x_b-curve $\varphi \mapsto x_b\left(\overline{\theta}(\varphi)\right)$ is outside the unit disk, and in Figure 3b, it meets the object.

Figure 3a provides a reconstruction with the data set defined by $c = 1.3$ in (4.2). Many artifacts in the reconstruction region are the same as in Figure 2 because the boundaries of the cutoff regions are substantially the same: the artifacts corresponding to the circles with $\varphi = 4\pi/9$ and the lower circle with $\varphi = 5\pi/9$ are the same limited-angle artifacts as in Figure

2 because those parts of the boundaries are the same. However, the upper right circled point in the sinogram has $\varphi > 5\pi/9$, so the corresponding artifact line has this larger angle, as seen in the reconstruction. The center reconstruction in Figure 3a shows the x_b-curve of artifacts, but it is far enough from D that it is not visible in the reconstruction on the right.

Figure 3b provides a reconstruction with the data set defined by $c = 0.65$ in (4.2). In this case, the object-dependent artifacts are similar to those in Figure 3a, but the lines for (φ, p) defined by (4.2) are different because $\mathrm{bd}(\widetilde{A})$ is different. The highlighted part of the boundary of $\widetilde{A}$ defined by (4.2) indicates the boundary points that create the part of the x_b-curve of artifacts that now meets the reconstruction region. The highlighted curve in the right-hand reconstruction of Figure 3b is this part of the x_b-curve. Note that this curve is calculated using the formula (3.6) for $x_b\left(\overline{\theta}(\varphi)\right)$ rather than by visually tracing the physical curve on the reconstruction. The fact that the calculated curve and the artifact curve are substantially the same shows the efficacy of our theory. A simple exercise shows that, for any $c > 0$, the x_b-curve changes direction at $x_b(\overline{\theta}(1/2 + 5\pi/9))$.

Let (φ_0, p_0) be the coordinates of the circled point in the upper right of the sinogram in Figure 3b. This circled point is on the boundary of $\mathrm{supp}(Rf)$, so $\widetilde{L}(\varphi_0, p_0)$ is tangent to the skull and an object-dependent artifact is visible on $\widetilde{L}(\varphi_0, p_0)$ in the reconstruction. The x_b-curve ends at $x_b\left(\overline{\theta}(\varphi_0)\right)$ (as justified by Theorem 3.4B.), and so the x_b-curve seems to blend into this line $\widetilde{L}(\varphi_0, p_0)$. If $\mathrm{supp}(f)$ were larger and the dotted part of the magenta curve on the sinogram were in $\mathrm{supp}(Rf)$, the x_b-curve would be longer.

4.3. Region-of-interest (ROI) tomography. The ROI problem, also known as interior tomography, is a classical incomplete data tomography problem in which a part of the object (the ROI) is imaged using only data over lines that meet the ROI. Such ROI data are generated, e.g., when the detector width is not large enough to contain the complete object or when researchers would like a higher resolution scan of a small part of the object. In this section, we apply our theorems to understand ROI CT microlocally, including the ring artifact at the boundary of the ROI. We should point out that practitioners are well aware of the ring artifacts (see, e.g., [8, 11]). Important related work has been done to analyze the ROI problem (see, e.g., [12, 13, 26, 29, 47, 51]).

First, note that Theorem 3.4C. implies that all singularities of f in the interior of the ROI are recovered. This is observed in Figure 4. If the ROI were not convex, then all singularities in the interior of its convex hull would be visible.

The boundary of the sinogram in Figure 4 is given by horizontal lines $p = \pm 0.8$. Since $p' = 0$, the x_b-curve (3.6) is given by $x_b\left(\overline{\theta}(\varphi)\right) = 0.8 \cdot \overline{\theta}(\varphi)$, which is a circle of radius 0.8. The x_b-artifact-circle is highlighted in the right reconstruction of Figure 4, but it can also be seen clearly in the top and bottom of the center reconstruction, even without the highlighting. However, the artifact circle does not extend outside the object (as represented by the dotted magenta curve in the reconstruction and which comes from the dotted segments of $\mathrm{bd}(\widetilde{A})$ in the sinogram) because Rf is zero near the corresponding lines. Theorem 3.5 B(2) can be used to explain the invisible curve.

One also sees object-dependent artifacts described by Theorem 3.7A. in Figure 4. For example, streak artifacts occur on the lines $\widetilde{L}(\varphi_0, p_0)$ corresponding to the four circled points (φ_0, p_0) in $\mathrm{bd}(\widetilde{A})$ in the sinogram. These lines $\widetilde{L}(\varphi_0, p_0)$ are tangent to the outer boundary of

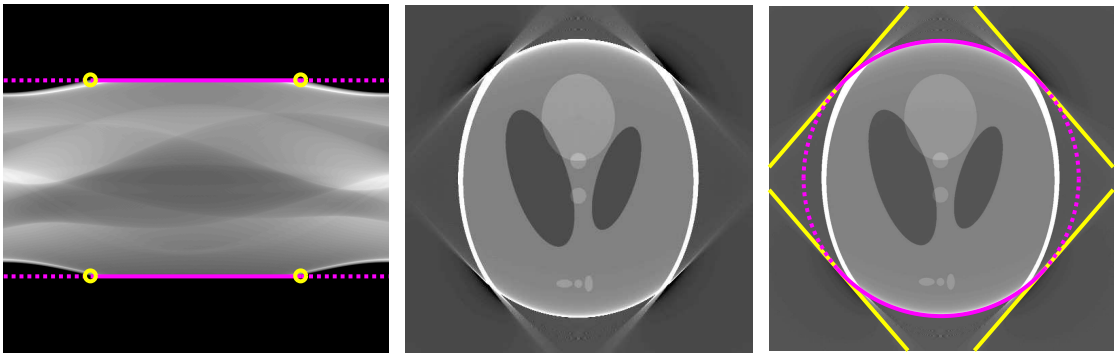

Figure 4. *Left: ROI data taken within a disk of radius* 0.8 *centered at the origin,* $p \in [-0.8, 0.8]$. *The boundary of* $\widetilde{A}$ *is highlighted in magenta. Center: FBP reconstruction. Right: Same FBP reconstruction as in the center image, highlighting the* x_b*-curve of artifacts in magenta and the object-dependent streak artifacts in yellow.*

the skull, and therefore f has wavefront set directions normal to these lines, and this causes the artifacts by Theorem 3.7A.

In general, one can show that if the ROI is strictly convex with a smooth boundary, then the x_b-curve of artifacts traces the boundary of the ROI. The proof is an exercise using the parameterization in (φ, p) of tangent lines to this boundary.

4.4. The general case. The reconstruction in Figure 5 illustrates all of our cases in one. In that figure, we consider a general incomplete data set with a rectangular region cut out of the sinogram leading to all considered types of artifacts. Now, we describe the resulting artifacts. In Figure 5, the horizontal sinogram boundaries at $p = p_0 = \pm 0.35$ for $\phi \in \left[\frac{7}{18}\pi, \frac{11}{18}\pi\right]$ are displayed with a solid magenta line. As in the ROI case, on these boundaries, we have $p' = 0$, and thus circular arcs of radius p_0 for the given interval for φ are added in the reconstruction (as indicated by solid magenta). As predicted by Theorem 3.7C., each of the four corners

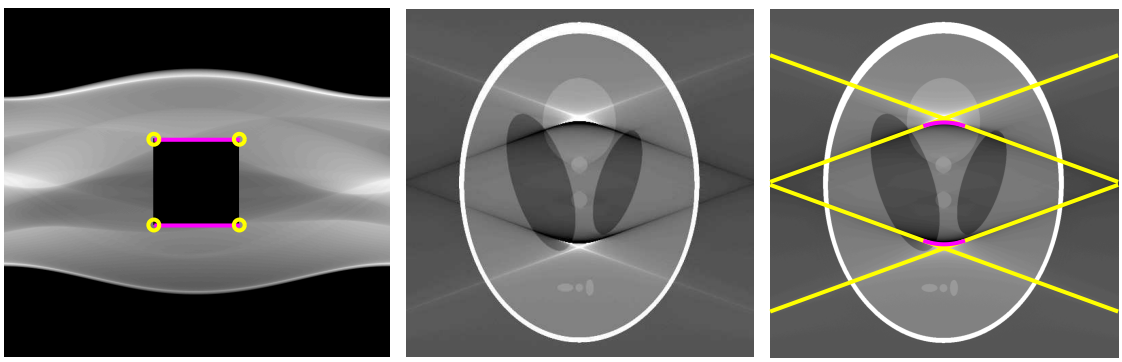

Figure 5. *Left: The sinogram for a general incomplete data problem in which the cutoff region,* $\widetilde{A}$*, has a locally smooth boundary with zero and infinite slope as well as corners. The cutout from the sinogram is at* $\frac{7\pi}{18}$ *and* $\frac{11\pi}{18}$*,* $p = \pm 0.35$. *Center: FBP reconstruction. Right: Same reconstruction with the circular* x_b*-curve of artifacts highlighted in magenta and object-independent "corner" streak artifacts highlighted in yellow.*

produces a line artifact as marked by the yellow solid lines in the right-hand reconstruction, and they align tangentially with the ends of the curved artifacts.

The circular arc between those lines corresponds to the top and bottom parts of $\mathrm{bd}(\widetilde{A})$ as the data are, locally, constrained as in ROI CT (see section 4.3).

In Figure 5, there are other object-dependent streaks corresponding to the vertical lines in the sinogram at $\varphi = \frac{7\pi}{18}$ and at $\varphi = \frac{11\pi}{18}$ as predicted by Theorem 3.7A., but they are less pronounced and more difficult to see.

4.5. Summary. We have presented reconstructions that illustrate all types of incomplete data and each of our theorems from section 3. All artifacts arise because of points $(\varphi_0, p_0) \in \mathrm{bd}(\widetilde{A})$, and they fall into two categories:

- Streak artifacts on the line $\widetilde{L}(\varphi_0, p_0)$.
  - Object-dependent streaks occur when $\mathrm{bd}(\widetilde{A})$ is smooth at (φ_0, p_0) and a singularity of f is normal to $\widetilde{L}(\varphi_0, p_0)$.
  - Object-independent streaks occur when $\mathrm{bd}(\widetilde{A})$ is nonsmooth at (φ_0, p_0).
- Artifacts on curves are always object-independent, and they are generated by the map $\varphi \mapsto x_b\left(\overline{\theta}(\varphi)\right)$ from parts of $\mathrm{bd}(\widetilde{A})$ that are smooth and of small slope.

5. Strength of added artifacts. In this section, we go back to parameterizing lines by $(\theta, p) \in S^1 \times \mathbb{R}$.

Using the Sobolev continuity of Rf, one can measure the strength in Sobolev scale of added artifacts in several useful cases. First, we define the Sobolev norm [45, 53]. We state it for distributions; therefore, it will apply to functions $f \in L^2_{\mathrm{loc}}(D)$.

Definition 5.1 (Sobolev wavefront set [45]). *For $s \in \mathbb{R}$, the Sobolev space $H_s(\mathbb{R}^n)$ is the set of all distributions with a locally square-integrable Fourier transform and with a finite Sobolev norm:*

$$\|f\|_s := \left(\int_{y\in\mathbb{R}^n} |\mathcal{F}f(y)|^2 \left(1 + \|y\|^2\right)^s dy\right)^{1/2} < \infty. \tag{5.1}$$

Let f be a distribution, and let $x_0 \in \mathbb{R}^n$ and $\xi_0 \in \mathbb{R}^n \setminus \mathbf{0}$. We say f is in H^s at x_0 in direction ξ_0 if there are a cutoff function ψ at x_0 and an open cone V containing ξ_0 such that the localized and microlocalized Sobolev seminorm *is finite:*

$$\|f\|_{s,\psi,V} := \left(\int_{y\in V} \left|\mathcal{F}\left(\psi f\right)(y)\right|^2 \left(1 + \|y\|^2\right)^s dy\right)^{1/2} < \infty. \tag{5.2}$$

If (5.2) does not hold for any cutoff function at x_0, ψ, or any conic neighborhood V of ξ_0, then we say that (x_0, ξ_0) is in the Sobolev wavefront set of f of order s, $(x_0, \xi_0) \in \mathrm{WF}_s(f)$.

An exercise using the definitions shows that $\mathrm{WF}(f) = \cup_{s\in\mathbb{R}} \mathrm{WF}_s(f)$ (see [15]).

The Sobolev wavefront set can be defined for measurable functions g on $S^1 \times \mathbb{R}$ using the identification (2.6) that reduces to this definition for $\widetilde{g}(\varphi, p) = g\left(\overline{\theta}(\varphi), p\right)$.

Note that this norm on distributions on $S^1 \times \mathbb{R}$ is not the typical $H_{0,s}$ norm used in elementary continuity proofs for the Radon transform (see, e.g., [22, equation (2.11)]), but this is the appropriate norm for the continuity theorems for general FIOs [23, Theorem 4.3.1], [10, Corollary 4.4.5].

Our next theorem gives the strength in Sobolev scale of added singularities of $\mathcal{L}_A f$ under certain assumptions on f. It uses the relation between the microlocal Sobolev strength of f and Rf [47, Theorem 3.1], and of g and R^*g, which is given in Proposition A.6 (see also [29] for related results).

Theorem 5.2. *Let $f \in L^2(D)$, and let $A \subset S^1 \times \mathbb{R}$ satisfy Assumption 3.1. Let $(\theta_0, p_0) \in \mathrm{bd}(A)$, and assume $Rf(\theta_0, p_0) \neq 0$ and f is smooth normal to $L(\theta_0, p_0)$, i.e., $\mathrm{WF}_{L(\theta_0,p_0)}(f) = \emptyset$.*

A. *Assume $\mathrm{bd}(A)$ is smooth and not vertical at (θ_0, p_0). Let $x_b = x_b(\theta_0)$ be given by (3.6), and let $\omega \neq 0$. Then, $\mathcal{L}_A f$ is in H_s for $s < 0$ at $\xi_0 = (x_b, \omega\bar{\theta}(\theta_0))$ and $\xi_0 \in \mathrm{WF}_0(\mathcal{L}_A f)$. Thus, there are singularities above x_b in the 0-order wavefront set of $\mathcal{L}_A f$.*

B. *Now, assume $\mathrm{bd}(A)$ has a corner at (θ_0, p_0) (see Definition 3.2). Then, for each $(x, \xi) \in N(L(\theta_0, p_0))$, $(x, \xi) \in \mathrm{WF}_1(\mathcal{L}_A f)$ and, except for two points on $L(\theta_0, p_0)$, $\mathcal{L}_A f$ is in H_s for $s < 1$ at (x, ξ). If one of the two one-sided tangent lines to the corner is vertical, then there is only one such point.*

This theorem provides estimates on smoothness for more general data sets than the limited-angle case, which was thoroughly considered in [25, 36]. In contrast to part A., if $\mathrm{bd}(A)$ has a vertical tangent at (θ_0, p_0), then, under the smoothness assumption on f, there are no added artifacts in $\mathcal{L}_A f$ normal to $L(\theta_0, p_0)$ (see Theorem 3.7A.). Part A. is a more precise version of Theorem 3.5B(3). Under the assumptions in parts A. and B., $\mathrm{bd}(A)$ *will cause* specific singularities in specific locations on $L(\theta_0, p_0)$. The two more singular points in part B. are specified in (A.15). If one part of $\mathrm{bd}(A)$ is vertical at (θ_0, p_0), then there is only one such more singular point.

This theorem will be proven in Appendix A.3.

6. Artifact reduction.

In this section, we briefly describe a method to suppress the added streak artifacts described in Theorems 3.5 and 3.7. This is a standard technique for many practitioners, but it is worth highlighting because it is simple and useful.

As outlined in section 3, the application of FBP to incomplete data extends the data from $A \subset S^1 \times \mathbb{R}$ to all of $S^1 \times \mathbb{R}$ by padding it with zeros on the complement of A. This hard truncation can create discontinuities on $\mathrm{bd}(A)$, and that explains the artifacts. These jumps are stronger singularities than those of Rf for $Rf \in H_{1/2}(S^1 \times \mathbb{R})$ since $f \in L^2(D) = H_0(D)$.

One natural way to get rid of the jump discontinuities of $\mathbb{1}_A$ is to replace $\mathbb{1}_A$ by a smooth function on $S^1 \times \mathbb{R}$, ψ, that is equal to zero off of A and equal to one on most of $\mathrm{int}(A)$ and smoothly transitions to zero near $\mathrm{bd}(A)$. We also assume ψ is symmetric in the sense that $\psi(\theta, p) = \psi(-\theta, -p)$ for all (θ, p). This gives the forward operator

$$R_\psi f(\theta, p) = \psi(\theta, p) Rf(\theta, p) \tag{6.1}$$

and the reconstruction operator

$$\mathcal{L}_\psi f = R^* \left(\Lambda R_\psi f\right) = R^* \left(\Lambda \psi Rf\right). \tag{6.2}$$

Because ψ is a smooth function, R_ψ is a standard FIO, and so $\mathcal{L}_\psi$ is a standard pseudodifferential operator. This allows us to show that $\mathcal{L}_\psi$ does not add artifacts.

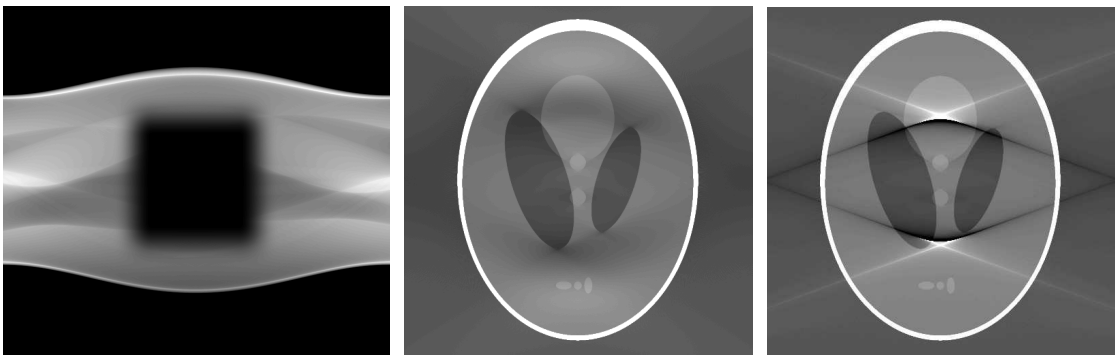

Figure 6. *Left: Smoothed sinogram. Center: Smoothed reconstruction with suppressed artifacts. Right: Reconstruction using $\mathcal{L}_A$ with sharp cutoff.*

Theorem 6.1 (artifact reduction theorem). *Let $f \in L^2(D)$, and let $A \subset S^1 \times \mathbb{R}$ satisfy Assumption 3.1. Then,*

$$\mathrm{WF}(\mathcal{L}_\psi f) \subset \mathrm{WF}(f). \tag{6.3}$$

Therefore, $\mathcal{L}_\psi$ does not add artifacts to the reconstruction.

Let $x \in D$, $\theta \in S^1$, and $\omega \neq 0$. If $\psi(\theta, x \cdot \theta) \neq 0$, then

$$(x, \omega\theta) \in \mathrm{WF}(\mathcal{L}_\psi f) \quad \textit{if and only if} \quad (x, \omega\theta) \in \mathrm{WF}(f). \tag{6.4}$$

Theorem 6.1 is a special case of a known result in, e.g., [29] or the symbol calculation in [46] and is stated for completeness. This theorem shows the advantages of including a smooth cutoff, and it has been suggested in several settings, including limited-angle X-ray CT [16, 25] and more general tomography problems [17, 18, 29, 54]. More sophisticated methods are discussed in [6, 7] for the synchrotron problem that is described in section 7.

Although this artifact reduction technique does not create any *singular* artifacts in $\mathcal{L}_\psi f$, it can turn *singular* artifacts into *smooth* artifacts, for example, by smoothing x_b-curves.

Figure 6 illustrates the efficacy of this smoothing algorithm on simulated data, and Figure 9 in section 8 demonstrates its benefits on real synchrotron data.

7. Application: A synchrotron experiment.

In this section, we use the identifications given in (4.1) and show sinograms as subsets of the (φ, p)-plane.

Figure 7 shows tomographic data of a chalk sample (sinogram on the left and a zoomed version in the center) that was acquired by a synchrotron experiment [6, 7] (see [30] for related work). In the right picture of Figure 7, a zoom of the corresponding reconstruction is shown (see also Figure 9a). As can be clearly observed, the reconstruction includes dramatic streaks that are independent of the object. These streaks motivated the research in this article since they were not explained by the mathematical theory at that time (such as in [16, 17, 18, 25, 36]).

Taking a closer look at the attenuation sinogram and its zoom in Figure 7, a staircasing is revealed with vertical and horizontal boundaries. This is a result of X-rays being blocked by

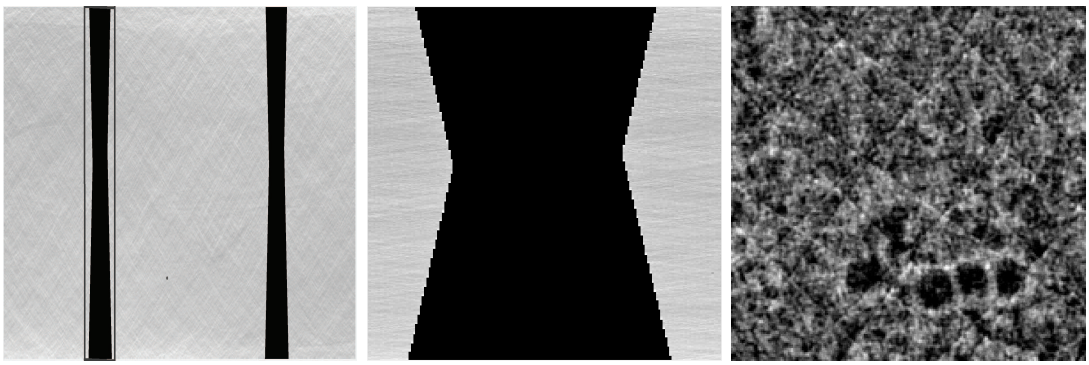

Figure 7. *Left: The truncated attenuation sinogram (after processing to get Radon transform data). Center: The enlargement of the section of* $\mathrm{bd}(\widetilde{A})$ *between the two dark vertical lines in the left-hand sinogram. Right: Zoom of the corresponding reconstruction.* [6, ©*IOP Publishing. Reproduced by permission of IOP Publishing. All rights reserved.*]

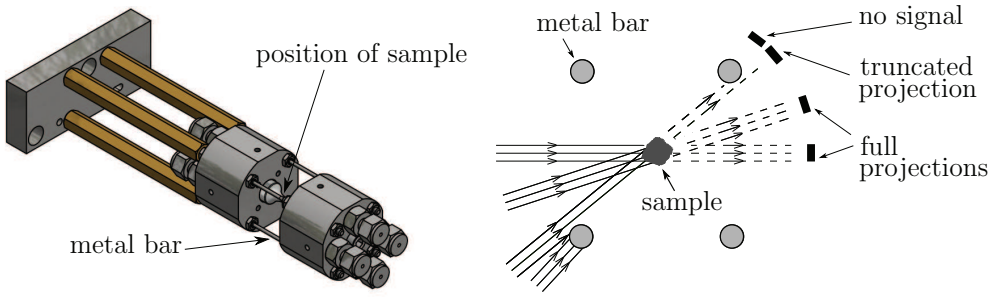

Figure 8. *Data acquisition setup for the synchrotron experiment* [6, ©*IOP Publishing. Reproduced by permission of IOP Publishing. All rights reserved.*]

four metal bars that help stabilize the percolation chamber (sample holder) as the sample is subjected to high pressure during data acquisition; see Figure 8. More details are given in [6].

Because the original reconstructions of this synchrotron data used a sharp cutoff, $\mathbb{1}_A$, the reconstructions suffer from severe streak artifacts, as can be seen in Figure 9a. These artifacts are exactly described by Theorem 3.7C., in that each corner of the sinogram gives rise to a line artifact in the reconstruction (cf. the left and center images in Figure 7). The authors of [6] then use a smooth cutoff function at $\mathrm{bd}(\widetilde{A})$ that essentially eliminates the streaks. The resulting reconstruction is shown in Figure 9b.

8. Discussion.

We first make observations about our results for $\mathcal{L}_A$ and then discuss generalizations.

8.1. Observations.

The proofs of Theorems 3.5 and 3.7 show that if $(\theta_0, p_0) \in \mathrm{bd}(A)$ and $\mathrm{WF}(\mathbb{1}_A Rf) = T^*(S^1 \times \mathbb{R}) \setminus \mathbf{0}$, then $\mathcal{L}_A f$ will have a streak all along $L(\theta_0, p_0)$. The analogous theorem for Sobolev singularities, Theorem 5.2B., assumes that A has a corner at (θ_0, p_0). If A has a weaker singularity at (θ_0, p_0), then an analogous theorem would hold, but one would need to factor in the Sobolev strength of the wavefront of $\mathbb{1}_A$ above (θ_0, p_0).

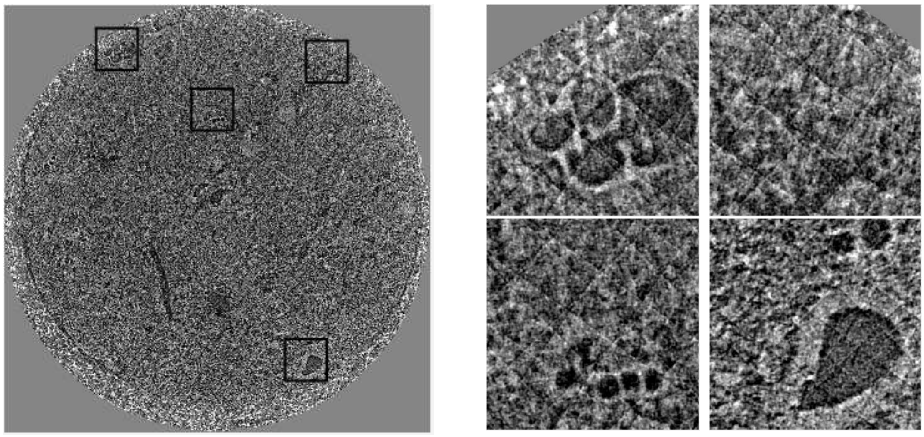

(a) Standard FBP reconstruction.

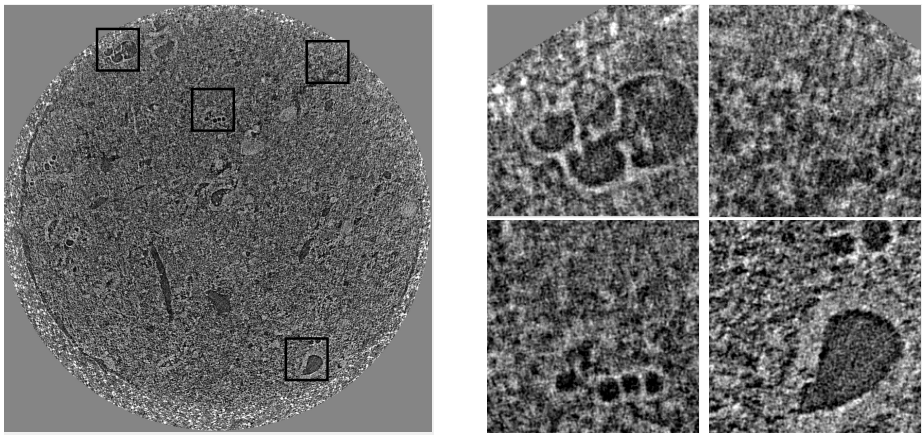

(b) FBP reconstruction with artifact reduction (cf. Theorem 6.1).

Figure 9. *Reconstructions from synchrotron data without smoothing (top) and with smoothing (bottom)* [6, ©*IOP Publishing. Reproduced by permission of IOP Publishing. All rights reserved.*]

The artifact reduction method, which is motivated by Theorem 6.1, works well for the synchrotron data, as shown in Figure 9. The article [6] provides more elaborate artifact reduction methods that are even more successful for this particular problem. We point out that this simple technique might not work as efficiently in other incomplete data tomography problems as in the problems we present. Nevertheless, our theorems and experiments show that abrupt cutoffs that add new singularities in the sinogram should be avoided.

There are other methods to deal with incomplete data. For example, data completion using the range conditions for the Radon transform has been developed, e.g., in [2, 3, 31, 57]. In [39] and [9, 42], the authors develop artifact reduction methods for quantitative susceptibility mapping. For metal artifacts, there is vast literature (see, e.g., [4]) for artifact reduction

methods, and we believe that those methods might also be useful for certain other incomplete data tomography problems. In [40, 44, 52], the authors have effectively used microlocal analysis to understand these related problems.

Our theory is developed based on the continuous case—we view the data as a function on $S^1 \times \mathbb{R}$, not just defined at discrete points. As shown in this article, our theory predicts and explains the artifacts and visible and invisible singularities. In practice, real data are discrete, and discretization may also introduce artifacts, such as undersampling streaks. Discretization in our synchrotron experiment could be a factor in the streaks in Figure 7 in section 7. Furthermore, numerical experiments have finite resolution, and this can cause (and sometimes de-emphasize) artifacts. For all these reasons, further analysis is needed to shed light on the interplay between the discrete and the continuous theories for CT reconstructions from incomplete data.

8.2. Generalizations. Theorems 3.5 and 3.7 were proven for $\mathcal{L}_A = R^* (\Lambda (\mathbb{1}_A R))$, but the results hold for any filtering operator that is elliptic in the sense of Remark A.5. This is true because that ellipticity condition is all we used about Λ in the proofs. For example, the operator, $L = -\frac{\partial^2}{\partial p^2}$, in Lambda CT [13] satisfies this condition, and the only difference comes in our Sobolev continuity theorem (Theorem 5.2). Since L is order two, the operator $R^* L R$ is of order 1 and the smoothness in Sobolev scale of the reconstructions would be one degree lower than for $\mathcal{L}_A$.

Our theorems hold for fan-beam data when the source curve γ is smooth and convex and the object is compactly supported inside γ. This is true because, in this case, the fan-beam parameterization of lines is diffeomorphic to the parallel-beam parameterization we use and the microlocal theorems we use are invariant under diffeomorphisms. However, one needs to check that the parallel-beam data set equivalent to the given fan-beam data set satisfies Assumption 3.1.

Theorems 3.5 and 3.7 hold verbatim for generalized Radon transforms with smooth measures on lines in $\mathbb{R}^2$ because they all have the same canonical relation, given by (A.4), and the proofs would be done as for $\mathcal{L}_A$ but using the basic microlocal analysis in [46].

Analogous theorems hold for other Radon transforms including the generalized hyperplane transform, the spherical transform of photoacoustic CT, and other transforms satisfying the Bolker assumption (A.7). The proofs would use our arguments here plus the proofs in [17, 18]. These generalizations are the subject of ongoing work. In incomplete data problems for R, either the artifacts are on x_b-curves or they are streaks on the lines corresponding to points on $\mathrm{bd}(A)$. However, in higher-dimensional cases, the results will be more subtle because artifacts can spread on *proper subsets* of the surface over which data are taken, not necessarily the entire set (see [17, Remark 4.7]).

Analogous theorems should hold for cone-beam CT, but this type of CT is more subtle because the reconstruction operator itself can add artifacts, even with complete data [14, 19].

Appendix A. Proofs. We now provide some basic microlocal analysis and then use this to prove our theorems. We adapt the standard terminology of microlocal analysis and consider wavefront sets as subsets of cotangent spaces [58]. Elementary presentations of microlocal analysis for tomography are in [27, 28]. Standard references include [15, 56].

A.1. Building blocks. Our first lemma gives some basic facts about wavefront sets.

Lemma A.1. *Let $x_0 \in \mathbb{R}^2$. Let u and v be locally integrable functions or distributions:*

A. *Let U be an open neighborhood of x_0. Assume that u and v are equal on U; then $\mathrm{WF}_{x_0}(u) = \mathrm{WF}_{x_0}(v)$.*
B. *If u and ψ are both in L^2_{loc} and ψ is smooth near x_0, then $\mathrm{WF}_{x_0}(\psi u) \subset \mathrm{WF}_{x_0}(u)$. If, in addition, ψ is nonzero at x_0, then $\mathrm{WF}_{x_0}(u) = \mathrm{WF}_{x_0}(\psi u)$.*
C. *$\mathrm{WF}_{x_0}(u) = \emptyset$ if and only if there is an open neighborhood U of x_0 on which u is a smooth function.*

The analogous statements hold for functions on $S^1 \times \mathbb{R}$.

These basic properties are proven using the arguments in section 8.1 of [24], in particular Lemma 8.1.1, Definition 8.1.2, and Proposition 8.1.3. This lemma is valid for functions on $S^1 \times \mathbb{R}$ using the identifications of $S^1 \times \mathbb{R}$ with $\mathbb{R}^2$ given by (2.5) and for functions (2.6), as well as the fact that singularities are defined locally.

Our next definition will be useful for describing how wavefront sets transform under R and R^*.

Definition A.2. *Let $C \subset T^*(S^1 \times \mathbb{R}) \times T^*(\mathbb{R}^2)$, and let $B \subset T^*(\mathbb{R}^2)$. The composition is defined as*

$$C \circ B = \left\{(\theta, p, \eta) \in T^*(S^1 \times \mathbb{R}) : (\theta, p, \eta, x, \xi) \in C \text{ for some } (x, \xi) \in B\right\}.$$

We define $C^t = \{(x, \xi, \theta, p, \eta) : (\theta, p, \eta, x, \xi) \in C\}$.

The function g on $S^1 \times \mathbb{R}$ will be called *symmetric* if

$$\forall (\theta, p) \in S^1 \times \mathbb{R},\ g(\theta, p) = g(-\theta, -p). \tag{A.1}$$

If $f \in L^2(D)$, then Rf and $\Lambda \mathbb{1}_A Rf$ are both locally integrable functions and are symmetric in this sense. For such functions,

$$(\theta_0, p_0, \omega_0(-\alpha \mathrm{d}\theta + \mathrm{d}p)) \in \mathrm{WF}(g) \Leftrightarrow (-\theta_0, -p_0, -\omega_0(\alpha \mathrm{d}\theta + \mathrm{d}p)) \in \mathrm{WF}(g). \tag{A.2}$$

For these reasons, we will identify cotangent vectors

$$(\theta_0, p_0, \omega_0(-\alpha \mathrm{d}\theta + \mathrm{d}p)) \Leftrightarrow (-\theta_0, -p_0, -\omega_0(\alpha \mathrm{d}\theta + \mathrm{d}p)). \tag{A.3}$$

Our next proposition is the main technical theorem of the article. It provides the wavefront correspondences for R and R^* which we will use in our proofs.

Proposition A.3 (microlocal correspondence of singularities). *The X-ray transform R is an elliptic FIO with canonical relation*

$$\begin{aligned} C = \Big\{ &\Big(\theta, x \cdot \theta, \omega(-x \cdot \theta^{\perp} \mathrm{d}\theta + \mathrm{d}p), x, \omega \theta \mathrm{d}x\Big) \\ &: \theta \in S^1,\ x \in \mathbb{R}^2,\ \omega \neq 0\Big\}. \end{aligned} \tag{A.4}$$

Let $f \in L^2(D)$, and let g be a locally integrable function on $S^1 \times \mathbb{R}$ that is symmetric by (A.1). Let $x_0 \in \mathbb{R}^2$, let $\theta_0 \in S^1$, and let p, α, and ω be real numbers with $\omega \neq 0$.

The X-ray transform R is an elliptic FIO with canonical relation C. Therefore,

$$\begin{gathered}\mathrm{WF}(Rf) = C \circ \mathrm{WF}(f), \quad \textit{where} \\ C \circ \{(x_0, \omega\theta \mathrm{dx})\} = \left\{ \left(\theta_0, x_0 \cdot \theta_0, \omega(-x_0 \cdot \theta_0^{\perp} \mathrm{d}\theta + \mathrm{dp}) \right) \right\}\end{gathered} \tag{A.5}$$

under the identification (A.3).

The dual transform R^* is an elliptic FIO with canonical relation C^t. Then,

$$\begin{gathered}\mathrm{WF}(R^* g) = C^t \circ \mathrm{WF}(g), \quad \textit{where} \\ C^t \circ \{(\theta, p, \omega(-\alpha \mathrm{d}\theta + \mathrm{dp}))\} = \{(x_0(\theta, p, \alpha), \omega\theta \mathrm{dx})\} \\ \textit{and} \quad x_0(\theta, p, \alpha) = \alpha\theta^{\perp} + p\theta.\end{gathered} \tag{A.6}$$

Here are pointers to the elements of this proof. The facts about R are directly from [47, Theorem 3.1] or [49, Theorem A.2], and they use the calculus of the FIO R [20, 21] (see also [46]). Note that the crucial point is that R is an elliptic FIO that satisfies the *global Bolker assumption:* the natural projection

$$\Pi_L : C \to T^*(Y) \text{ is an injective immersion,} \tag{A.7}$$

so (A.5) holds for R. A straightforward calculation using (A.4) shows that the global Bolker assumption holds. Note that we are using the identification (A.3) in asserting that (A.5) is an equality. The proofs for R^* are parallel to those for R, except they involve the canonical relation for R^*, C^t rather than C.

Remark A.4. In [17, 18], the authors prove artifact characterizations for limited data problems for photoacoustic CT and generalized hyperplane transforms. One key is a fundamental result on multiplying distributions [24, Theorem 8.2.10]. If u and v are distributions on $S^1 \times \mathbb{R}$, this theorem implies they can be multiplied *as distributions* if they satisfy the following noncancellation condition: for all $(\theta, p, \eta) \in \mathrm{WF}(u)$, $(\theta, p, -\eta) \notin \mathrm{WF}(v)$. Then, uv is a distribution and an upper bound for $\mathrm{WF}(uv)$ is given in terms of $\mathrm{WF}(u)$ and $\mathrm{WF}(v)$.

However, this noncancellation condition does not hold for $\mathbb{1}_A$ and Rf when $\mathbb{1}_A$ is either smooth with small slope or is not smooth at (θ_0, p_0). That is why we consider functions $f \in L^2(D)$ in this article since $\mathbb{1}_A Rf$ will be a function in $L^2(S^1 \times \mathbb{R})$ even if [24, Theorem 8.2.10] does not apply.

Our next remark will be used in the ellipticity proofs that follow.

Remark A.5. The operator Λ is elliptic in all cotangent directions except $\mathrm{d}\theta$ because the symbol of Λ is $|\tau|$, where τ is the Fourier variable dual to p. However, the $\mathrm{d}\theta$ direction will not affect our proofs. This is true because, for any function $f \in L^2(D)$, the covector $(\theta, p, \omega \mathrm{d}\theta)$ is not in $\mathrm{WF}(Rf)$ because $\mathrm{WF}(Rf) = C \circ \mathrm{WF}(f)$ (use the definition of composition and (A.4)). So, for each $f \in L^2(D)$, $\mathrm{WF}(\Lambda Rf) = \mathrm{WF}(Rf)$. Because $C^t \circ \{(\theta, p, \alpha \mathrm{d}\theta)\} = \emptyset$ by (A.4), even if $(\theta, \omega \mathrm{d}\theta) \in \mathrm{WF}(\mathbb{1}_A Rf)$, that covector will not affect the calculation of $C^t \circ \mathrm{WF}(\Lambda \mathbb{1}_A Rf)$. Therefore, Λ is elliptic on all cotangent directions that are preserved when composed with C^t, and these are all the directions we need in our proofs.

Our theorems will be valid for any pseudodifferential operator on $S^1 \times \mathbb{R}$ that is invariant under the symmetry condition (A.1) and satisfies this ellipticity condition (although the Sobolev results will depend on the order of the operator).

A.2. Proofs of Theorems 3.5, 3.7, and 3.9. In the proofs of these theorems, we use Proposition A.3 to analyze how multiplication by $\mathbb{1}_A$ adds singularities to the data Rf and then to the reconstruction $\mathcal{L}_A f$. We first make observations that will be useful in the proofs.

Let A satisfy Assumption 3.1, and let $f \in L^2(D)$. Let

$$G = \mathbb{1}_A Rf; \quad \text{then} \quad R^*\Lambda G = \mathcal{L}_A f.$$

By Remark A.5 and the statements in Proposition A.3,

$$\mathrm{WF}(\mathcal{L}_A f) = C^t \circ \mathrm{WF}(G). \tag{A.8}$$

Using the expression (A.4) for C, one can show for $(\theta_0, p_0) \in S^1 \times \mathbb{R}$ that

$$\begin{aligned} &C \circ (N^*(L(\theta_0,p_0)) \setminus \mathbf{0}) = T^*_{(\theta_0,p_0)}(S^1 \times \mathbb{R}) \setminus P, \\ &\text{where} \quad N^*(L(\theta_0,p_0)) = \{(x, \omega\theta_0 \mathrm{dx}) : x \in L(\theta_0,p_0),\ \omega \in \mathbb{R}\} \\ &\text{and} \quad P = \left\{(\theta, p, \omega \mathrm{d}\theta) : (\theta,p) \in S^1 \times \mathbb{R},\ \omega \in \mathbb{R}\right\}. \end{aligned} \tag{A.9}$$

Because $\mathrm{WF}(Rf) = C \circ \mathrm{WF}(f)$, (A.9) implies that if f is smooth conormal to $L(\theta_0, p_0)$, then Rf is smooth near (θ_0, p_0).

Using analogous arguments for C^t, one shows for $(\theta, p) \in S^1 \times \mathbb{R}$ that

$$C^t \circ \left(T^*_{(\theta_0,p_0)}(S^1 \times \mathbb{R}) \setminus \mathbf{0}\right) = N^*(L(\theta_0,p_0)) \setminus \mathbf{0}. \tag{A.10}$$

By (A.8), if G is smooth near (θ_0, p_0), then $\mathcal{L}_A f$ is smooth conormal to $L(\theta_0, p_0)$.

To start the proofs, let $f \in L^2(D)$ and let A be a data set satisfying Assumption 3.1. Theorem 3.4 establishes that if $(\theta_0, p_0) \notin \mathrm{bd}(A)$, then there are no artifacts in $\mathcal{L}_A f$ conormal to $L(\theta_0, p_0)$ (since $\mathrm{WF}_{L(\theta_0,p_0)}(\mathcal{L}_A f) \subset \mathrm{WF}_{L(\theta_0,p_0)}(f)$). Therefore, the only singular artifacts are on lines $L(\theta_0, p_0)$ for $(\theta_0, p_0) \in \mathrm{bd}(A)$.

Proof of Theorem 3.5. Assume $\mathrm{bd}(A)$ is smooth with finite slope at (θ_0, p_0). Therefore, there are an open neighborhood I of θ_0 and a smooth function $p = p(\theta)$ for $\theta \in I$ such that $(\theta, p(\theta)) \in \mathrm{bd}(A)$. A straightforward calculation shows for each $\theta \in I$ and each $\omega \neq 0$ that

$$\eta(\theta) = \left(\theta, p(\theta), \omega\left(-p'(\theta)\mathrm{d}\theta + \mathrm{dp}\right)\right)$$

is conormal to $\mathrm{bd}(A)$ at $(\theta, p(\theta))$. A calculation using (A.6) and (A.8) shows that

$$\eta(\theta) \in \mathrm{WF}(G) \quad \text{if and only if} \quad (x_b(\theta), \omega\theta \mathrm{dx}) \in WF(\mathcal{L}_A f), \tag{A.11}$$

where $x_b(\theta)$ is given by (3.6). Then, $(x_b(\theta_0), \omega\theta_0 \mathrm{dx})$ is the possible object-independent artifact that could occur on $L(\theta_0, p_0)$. Note that $x_b(\theta)$ is simply the x-projection of $C^t \circ N^*(\mathrm{bd}(A))$.

By taking the derivative $x_b'(\theta)$, one can show that the only case in which the x_b-curve is a subset of a line occurs when $\mathrm{bd}(A)$ is locally defined by lines through a point (e.g., for some $x_0 \in \mathbb{R}^2$, $\mathrm{bd}(A)$ is locally given by $p(\theta) = x_0 \cdot \theta$). However, in this case, (3.6) shows that the x_b-curve is the single point x_0. This proves part 3.5A.

If f has no singularities conormal to $L(\theta_0, p_0)$, then Rf is smooth near (θ_0, p_0), and so $\mathrm{WF}_{(\theta_0,p_0)}(G) \subset \mathrm{WF}_{(\theta_0,p_0)}(\mathbb{1}_A)$ by Lemma A.1B. This proves part 3.5B(1).

If Rf is zero in a neighborhood of (θ_0, p_0), then G is smooth near (θ_0, p_0), so, by the note below (A.10), $\mathcal{L}_A f$ is smooth conormal to $L(\theta_0, p_0)$. This proves part 3.5B(2).

If $Rf(\theta_0, p_0) \neq 0$, then $\mathrm{WF}_{(\theta_0,p_0)}(G) = \{\eta(\theta_0)\}$ by Lemma A.1B. Now, by (A.11),

$$(x_b(\theta_0), \omega\theta_0 \mathrm{dx}) \in \mathrm{WF}(\mathcal{L}_A f).$$

This proves part 3.5B(3) and finishes the proof of part 3.5B. ∎

Proof of Theorem 3.7. To prove part 3.7A., we make a simple observation. Singularities of f conormal to $L(\theta_0, p_0)$ can cause singularities in G only above (θ_0, p_0), and those can cause singularities of $\mathcal{L}_A f$ only conormal to $L(\theta_0, p_0)$.

Part 3.7B. follows from the fact that the conormal to $\mathrm{bd}(A)$ at θ_0 is $\omega \mathrm{d}\theta$ for $\omega \neq 0$, the fact that $C^t \circ \{(\theta, p, \omega \mathrm{d}\theta\} = \emptyset$, and the arguments in the proof of Theorem 3.5B(1).

Now, we assume $\mathrm{bd}(A)$ is not smooth at (θ_0, p_0).

The first observation is straightforward: if $\mathrm{bd}(A)$ is not smooth at (θ_0, p_0), then that singularity can cause singularities in G at (θ_0, p_0) which cause singularities of $\mathcal{L}_A f$ conormal to $L(\theta_0, p_0)$ (and nowhere else).

Assume f is smooth conormal to $L(\theta_0, p_0)$, $Rf(\theta_0, p_0) \neq 0$, and A has a corner at (θ_0, p_0) (see Definition 3.2). Then, by Lemma A.1, $\mathrm{WF}_{(\theta_0,p_0)}(G) = \mathrm{WF}_{(\theta_0,p_0)}(\mathbb{1}_A)$, which is equal to $T^*_{(\theta_0,p_0)}(S^1 \times \mathbb{R}) \setminus \mathbf{0}$. Therefore, by (A.10), $\mathrm{WF}_{L(\theta_0,p_0)}(\mathcal{L}_A f) = N^*(L(\theta_0, p_0)) \setminus \mathbf{0}$. This finishes the proof of Theorem 3.7. ∎

Proof of Theorem 3.9. Let $f \in L^2(D)$, and assume A satisfies Assumption 3.1. Theorem 3.4 establishes that artifacts are added in $\mathcal{L}_A f$ conormal to $L(\theta_0, p_0)$ only when $(\theta_0, p_0) \in \mathrm{bd}(A)$. Let $(\theta_0, p_0) \in \mathrm{bd}(A)$. Singularities of $G = \mathbb{1}_A Rf$ at (θ_0, p_0) come only from singularities of $\mathbb{1}_A$ or singularities of Rf at (θ_0, p_0). Therefore, singularities of $\mathcal{L}_A f$ conormal to $L(\theta_0, p_0)$ come only from singularities of $\mathbb{1}_A$ at (θ_0, p_0) or singularities of Rf at (θ_0, p_0).

The artifacts of $\mathcal{L}_A f$ caused by $\mathbb{1}_A$ are analyzed in the proofs of Theorem 3.5 and Theorem 3.7B. and 3.7C. The artifacts of $\mathcal{L}_A f$ caused by Rf are covered in Theorem 3.7A. This takes care of all singular artifacts for the continuous problem. ∎

A.3. Proof of Theorem 5.2. We first prove a proposition giving the correspondence between the Sobolev wavefront set and R^*.

Proposition A.6 (Sobolev wavefront correspondence for R and R^*). *Let $(\theta_0, p_0) \in S^1 \times \mathbb{R}$, $\omega_0 \neq 0$, and let s and α be real numbers. Let*

$$\eta_0 = \omega_0(-\alpha \mathrm{d}\theta + \mathrm{dp}), \quad x_0 = p_0\theta_0 + \alpha\theta_0^{\perp}, \quad \text{and} \quad \xi_0 = \omega_0\theta_0 \mathrm{dx}.$$

Let f be a distribution on $\mathbb{R}^2$, and let g be a distribution on $S^1 \times \mathbb{R}$. Then,

$$(x_0, \xi_0) \in \mathrm{WF}_s(f) \iff (\theta_0, p_0, \eta_0) \in WF_{s+1/2}(Rf), \tag{A.12}$$

$$(\theta_0, p_0, \eta_0) \in \mathrm{WF}_s(g) \iff (x_0, \xi_0) \in WF_{s+1/2}(R^* g). \tag{A.13}$$

Proof. Equivalence (A.12) is given in [47, Theorem 3.1]; however, the proof of the $\Leftarrow$ implication for R was left to the reader.

The proof of the $\Rightarrow$ implication of (A.13) is completely analogous to the proof given in [47] for R. For completeness, we will prove the $\Leftarrow$ implication of (A.13). Assume g is in H_s at

(θ_0, p_0, η_0). By [45, Theorem 6.1, p. 259], we can write $g = g_1 + g_2$, where $g_1 \in H_s$ and $(\theta_0, p_0, \eta_0) \notin \mathrm{WF}(g_2)$. The operator R^* is continuous in Sobolev spaces from H_s to $H^{\mathrm{loc}}_{s+1/2}$ by [56, Theorem VIII 6.1] since C^t is a local canonical graph. Therefore, $R^*g_1 \in H^{\mathrm{loc}}_{s+1/2}$. Since $(\theta_0, p_0, \eta_0) \notin \mathrm{WF}(g_2)$, $(x_0, \xi_0) \notin \mathrm{WF}(R^*g_2)$ by the wavefront correspondence (A.6). An exercise using Definition 5.1 and the Fourier transform shows that $R^*g = R^*g_1 + R^*g_2$ is in $H_{s+1/2}$ at (x_0, ξ_0). ∎

Proof of Theorem 5.2. Let $f \in L^2(D)$, and let A satisfy Assumption 3.1. Let $(\theta_0, p_0) \in \mathrm{bd}(A)$, and assume $Rf(\theta_0, p_0) \neq 0$ and f is smooth conormal to $L(\theta_0, p_0)$. Because f is smooth conormal to $L(\theta_0, p_0)$, $\mathrm{WF}_{(\theta_0,p_0)}(Rf) = \emptyset$, so Rf is smooth in a neighborhood of (θ_0, p_0) by Lemma A.1C. Since $Rf(\theta_0, p_0) \neq 0$, for each s,

$$(\mathrm{WF}_{s-1})_{(\theta_0,p_0)}(\Lambda \mathbb{1}_A Rf) = (\mathrm{WF}_s)_{(\theta_0,p_0)}(\mathbb{1}_A Rf) = (\mathrm{WF}_s)_{(\theta_0,p_0)}(\mathbb{1}_A); \tag{A.14}$$

the left-hand equality is true because Λ is an elliptic pseudodifferential operator of order one (except in the irrelevant direction $\mathrm{d}\theta$; see Remark A.4), and the right-hand equality is true by Lemma A.1B.

To prove part 5.2A., assume $\mathrm{bd}(A)$ is smooth and has finite slope at (θ_0, p_0). Because the Sobolev wavefront set is contravariant under diffeomorphism [56], we may assume $\mathrm{bd}(A)$ is a horizontal line, at least locally near (θ_0, p_0). Let $\eta_0 = \mathrm{dp}$. We claim that $(\theta_0, p_0, \pm\eta_0) \in \mathrm{WF}_{1/2}(\mathbb{1}_A)$ and, for $s < 1/2$, $\mathbb{1}_A$ is in H_s at $(\theta_0, p_0, \pm\eta_0)$. Furthermore, $\mathbb{1}_A$ is smooth in every other direction above (θ_0, p_0). The proofs of these two statements are now outlined. Using a product cutoff function $\psi = \psi_1(\theta)\psi_2(p)$ to calculate $\mathcal{F}(\psi \mathbb{1}_A)$ and several applications of integration by parts, one can show that this localized Fourier transform is of the form $S(\nu)T(\tau)$, where S is a smooth, rapidly decreasing function and T is $\mathcal{O}(1/|\tau|)$ (and not $\mathcal{O}(1/|\tau|^p$ for any $p > 1$). Therefore, $S(\nu)T(\tau)$ is rapidly decaying in all directions but the vertical one. This implies that $\mathbb{1}_A$ is in H_s for $s < 1/2$ at $(\theta_0, p_0, \pm\eta_0)$ and $(\theta_0, p_0, \pm\eta_0) \in \mathrm{WF}_{1/2}(\mathbb{1}_A)$. This also shows that this localized Fourier transform is rapidly decaying in all directions except $\pm\eta_0$. Now, using (A.14) one sees that $(\theta_0, p_0, \pm\eta_0) \in \mathrm{WF}_{-1/2}(\Lambda \mathbb{1}_A Rf)$; $\Lambda \mathbb{1}_A Rf$ is in H_s for $s < -1/2$ at $(\theta_0, p_0, \pm\eta_0)$; and $(\theta_0, p_0, \eta) \notin \mathrm{WF}(\Lambda \mathbb{1}_A Rf)$ for any η not parallel to η_0.

Now, by Proposition A.6, $\mathcal{L}_A f = R^* \Lambda \mathbb{1}_A Rf$ is in H_s at $(x_b(\theta_0), \pm\theta_0 \mathrm{dx})$ for $s < 0$ and

$$(x_b(\theta_0), \pm\theta_0 \mathrm{dx}) \in WF_0(\mathcal{L}_A f),$$

where $x_b(\theta_0)$ is given by (3.6). Using this theorem again, one sees that for any $x \in L(\theta_0, p_0)$, if $x \neq x_b(\theta_0)$, then

$$(x, \pm\theta_0 \mathrm{dx}) \notin \mathrm{WF}(\mathcal{L}_A f).$$

Therefore, the only covectors in $N^*(L(\theta_0, p_0)) \cap \mathrm{WF}(\mathcal{L}_A f)$ are $(x_b(\theta_0), \alpha\theta_0 \mathrm{dx})$ for $\alpha \neq 0$.

To prove part 5.2B., assume $\mathrm{bd}(A)$ has a corner at (θ_0, p_0). Let α_1 and α_2 be the slopes at (θ_0, p_0) of the two parts of $\mathrm{bd}(A)$. Let

$$\eta_j = -\alpha_j \mathrm{d}\theta + \mathrm{dp}, \quad x_{bj} = p_0\theta_0 + \alpha_j \theta_0^{\perp}, \qquad j = 1, 2. \tag{A.15}$$

An argument similar to the diffeomorphism/integration by parts argument in the last part of the proof is used. First, a diffeomorphism is used to transform the corner, so *locally* A becomes

$\overline{A} = \{(\theta, p) : \theta \geq 0, p \geq 0\}$. To do this, one uses Definition 3.2, footnote 4, and the inverse and implicit function theorems. Then, one uses a product cutoff $\psi = \psi_1(\theta)\psi_2(p)$ to calculate $\mathrm{WF}_s(\mathbb{1}_{\overline{A}})$ at $(0, 0)$. Then, the Fourier transform can be written as $\mathcal{F}\left(\psi \mathbb{1}_{\overline{A}}\right) = S(\nu)T(\tau)$, where $S(\nu) = \mathcal{O}(1/|\nu|)$ and $T(\tau) = \mathcal{O}(1/|\tau|)$. So, the localized Fourier transform is decreasing of order -1 in the dp (vertical) and dθ (horizontal) directions and -2 in all other directions.

Note that η_1 and η_2 are the images of dp and dθ under the diffeomorphism back to the original coordinates. By the contravariance of the Sobolev wavefront set under diffeomorphism and the assumption that Rf is smooth and nonzero near (θ_0, p_0), $(\theta_0, p_0, \pm\eta_j) \in \mathrm{WF}_{-1/2}(\Lambda \mathbb{1}_A Rf)$ and, for $s < -1/2$, $\Lambda \mathbb{1}_A Rf$ is in H_s at (θ_0, p_0, η_j). Other covectors are in $\mathrm{WF}_{1/2}(\Lambda \mathbb{1}_A Rf)$. One finishes the proof using (A.13).

This proof shows for $j = 1, 2$ that $C^t \circ \{(\theta_0, p_0, \eta_j)\} \in \mathrm{WF}_0(\mathcal{L}_A f)$, and these are the "more singular points" referred to after the statement of Theorem 5.2. If one part of $\mathrm{bd}(A)$ is vertical at (θ_0, p_0), then for one value of j, η_j is parallel to dθ and $C^t \circ \{(\theta_0, p_0, \eta_j)\} = \emptyset$, so there is only one point, not two, on $L(\theta_0, p_0)$ on which f is more singular. ∎

Acknowledgments. The authors thank the Japan Synchrotron Radiation Research Institute for the allotment of beam time on beamline BL20XU of SPring-8 (Proposal 2015A1147) that provided the raw data described in section 7. In addition, they thank the funding agencies listed in the title footnote of the article. Finally, they thank the four referees for important comments that greatly improved the exposition and theorems, in particular the statements and proofs of Theorems 3.5 and 3.7. Todd Quinto thanks John Schotland and Guillaume Bal for a stimulating discussion about multiplying distributions that relates to Remark A.4 and the reasons for considering only functions in this article. He thanks Plamen Stefanov for stimulating discussions about these results. He also thanks the Technical University of Denmark and DTU Compute for a wonderful semester during which this research was being done, and he is indebted to his colleagues there for stimulating, enjoyable discussions that influenced this work. Finally, he thanks the Tufts University Deans of Arts and Sciences for their support for his semester at DTU.

REFERENCES

[1] L. L. Barannyk, J. Frikel, and L. V. Nguyen, *On artifacts in limited data spherical radon transform: Curved observation surface*, Inverse Problems, 32 (2016), 015012.

[2] R. H. T. Bates and R. M. Lewitt, *Image reconstruction from projections.* III: *Projection completion methods (theory),* Optik, 50 (1978), pp. 189–204.

[3] R. H. T. Bates and R. M. Lewitt, *Image reconstruction from projections.* IV: *Projection completion methods (computational examples)*, Optik, 50 (1978), pp. 269–278.

[4] F. E. Boas and D. Fleischmann, *CT artifacts: Causes and reduction techniques*, Imaging Med., 4 (2012), pp. 229–240.

[5] J. Boman and E. T. Quinto, *Support theorems for real analytic Radon transforms*, Duke Math. J., 55 (1987), pp. 943–948.

[6] L. Borg, J. S. Jørgensen, J. Frikel, and J. Sporring, *Reduction of variable-truncation artifacts from beam occlusion during in situ x-ray tomography*, Meas. Sci. Technol., 28 (2017), 124004, https://doi.org/10.1088/1361-6501/aa8c27.

[7] L. Borg, J. S. Jørgensen, and J. Sporring, *Towards Characterizing and Reducing Artifacts Caused by Varying Projection Truncation*, Technical Report, Department of Computer Science, University of Copenhagen, Copenhagen, Denmark, 2017, http://static-curis.ku.dk/portal/files/181386847/teknisk_rapport_leise_borg1.pdf.

[8] R. Chityalad, K. R. Hoffmann, S. Rudina, and D. R. Bednareka, *Region of interest (ROI) computed tomography (CT): Comparison with full field of view (FFOV) and truncated CT for a human head phantom*, in Proceedings of the International Society for Optical Engineering, Proc. SPIE Int. Soc. Opt. Eng. 5745(1), 2005, pp. 583–590.

[9] J. K. Choi, H. S. Park, S. Wang, Y. Wang, and J. K. Seo, *Inverse problem in quantitative susceptibility mapping*, SIAM J. Imaging Sci., 7 (2014), pp. 1669–1689, https://doi.org/10.1137/140957433.

[10] J. J. Duistermaat, *Fourier Integral Operators*, Progr. Math. 130, Birkhäuser Boston, Boston, MA, 1996.

[11] M. E. Eldib, M. Hegazy, Y. J. Mun, M. H. Cho, M. H. Cho, and S. Y. Lee, *A ring artifact correction method: Validation by micro-CT imaging with flat-panel detectors and a 2D photon-counting detector*, Sensors, 17 (2017), 269.

[12] A. Faridani, D. V. Finch, E. L. Ritman, and K. T. Smith, *Local tomography* II, SIAM J. Appl. Math., 57 (1997), pp. 1095–1127, https://doi.org/10.1137/S0036139995286357.

[13] A. Faridani, E. L. Ritman, and K. T. Smith, *Local tomography*, SIAM J. Appl. Math., 52 (1992), pp. 459–484, https://doi.org/10.1137/0152026.

[14] D. V. Finch, I.-R. Lan, and G. Uhlmann, *Microlocal analysis of the restricted X-ray transform with sources on a curve*, in Inside Out, Inverse Problems and Applications, G. Uhlmann, ed., Math. Sci. Res. Inst. Publ. 47, Cambridge University Press, Cambridge, UK, 2003, pp. 193–218.

[15] F. G. Friedlander, *Introduction to the Theory of Distributions*, 2nd ed., Cambridge University Press, Cambridge, UK, 1998.

[16] J. Frikel and E. T. Quinto, *Characterization and reduction of artifacts in limited angle tomography*, Inverse Problems, 29 (2013), 125007.

[17] J. Frikel and E. T. Quinto, *Artifacts in incomplete data tomography with applications to photoacoustic tomography and sonar*, SIAM J. Appl. Math., 75 (2015), pp. 703–725, https://doi.org/10.1137/140977709.

[18] J. Frikel and E. T. Quinto, *Limited data problems for the generalized Radon transform in* $\mathbb{R}^n$, SIAM J. Math. Anal., 48 (2016), pp. 2301–2318, https://doi.org/10.1137/15M1045405.

[19] A. Greenleaf and G. Uhlmann, *Non-local inversion formulas for the X-ray transform*, Duke Math. J., 58 (1989), pp. 205–240.

[20] V. Guillemin, *On Some Results of Gelfand in Integral Geometry*, Proc. Sympos. Pure Math. 43, AMS, Providence, RI, 1985, pp. 149–155.

[21] V. Guillemin and S. Sternberg, *Geometric Asymptotics*, AMS, Providence, RI, 1977.

[22] M. G. Hahn and E. T. Quinto, *Distances between measures from 1-dimensional projections as implied by continuity of the inverse Radon transform*, Z. Wahrsch. Verw. Gebiete, 70 (1985), pp. 361–380.

[23] L. Hörmander, *Fourier integral operators*, I, Acta Math., 127 (1971), pp. 79–183.

[24] L. Hörmander, *The Analysis of Linear Partial Differential Operators: Distribution Theory and Fourier Analysis* I, Classics Math., Springer-Verlag, Berlin, 2003.

[25] A. Katsevich, *Local tomography for the limited-angle problem*, J. Math. Anal. Appl., 213 (1997), pp. 160–182.

[26] A. I. Katsevich and A. G. Ramm, *Pseudolocal tomography*, SIAM J. Appl. Math., 56 (1996), pp. 167–191, https://doi.org/10.1137/S0036139994266116.

[27] V. P. Krishnan and E. T. Quinto, *Microlocal analysis in tomography*, in Handbook of Mathematical Methods in Imaging, O. Scherzer, ed., Springer-Verlag, New York, Berlin, 2015, pp. 847–902.

[28] P. Kuchment, *The Radon Transform and Medical Imaging*, CBMS-NSF Regional Conf. Ser. in Appl. Math. 85, SIAM, Philadelphia, 2014, https://doi.org/10.1137/1.9781611973297.

[29] P. Kuchment, K. Lancaster, and L. Mogilevskaya, *On local tomography*, Inverse Problems, 11 (1995), pp. 571–589.

[30] F. Lauze, Y. Quéau, and E. Plenge, *Simultaneous reconstruction and segmentation of CT scans with shadowed data*, in Scale Space and Variational Methods in Computer Vision, F. Lauze, Y. Dong, and A. B. Dahl, eds., Springer, Cham, 2017, pp. 308–319.

[31] A. K. Louis, *Picture reconstruction from projections in restricted range*, Math. Methods Appl. Sci., 2 (1980), pp. 209–220.

[32] A. K. Louis, *Incomplete data problems in X-ray computerized tomography* I. *Singular value decomposition of the limited angle transform*, Numer. Math., 48 (1986), pp. 251–262.

[33] F. Natterer, *Efficient implementation of "optimal" algorithms in computerized tomography*, Math. Methods Appl. Sci., 2 (1980), pp. 545–555.
[34] F. Natterer, *The Mathematics of Computerized Tomography*, Classics Appl. Math. 32, SIAM, Philadelphia, 2001, https://doi.org/10.1137/1.9780898719284.
[35] F. Natterer and F. Wübbeling, *Mathematical Methods in Image Reconstruction*, SIAM, Philadelphia, 2001, https://doi.org/10.1137/1.9780898718324.
[36] L. V. Nguyen, *How strong are streak artifacts in limited angle computed tomography?*, Inverse Problems, 31 (2015), 055003.
[37] L. V. Nguyen, *On artifacts in limited data spherical Radon transform: Flat observation surfaces*, SIAM J. Math. Anal., 47 (2015), pp. 2984–3004, https://doi.org/10.1137/140980740.
[38] L. V. Nguyen, *On the strength of streak artifacts in filtered back-projection reconstructions for limited angle weighted x-ray transform*, J. Fourier Anal. Appl., 23 (2017), pp. 712–728.
[39] B. Palacios, G. Uhlmann, and Y. Wang, *Reducing streaking artifacts in quantitative susceptibility mapping*, SIAM J. Imaging Sci., 10 (2017), pp. 1921–1934, https://doi.org/10.1137/16M1096475.
[40] B. Palacios, G. Uhlmann, and Y. Wang, *Quantitative analysis of metal artifacts in X-ray tomography*, SIAM J. Math. Anal., 50 (2018), 4914–4936, https://doi.org/10.1137/17M1160392.
[41] V. Palamodov, *Nonlinear artifacts in tomography*, Soviet Phys. Dokl., 31 (1986), pp. 888–890.
[42] V. Palamodov, *A method of reduction of artifacts of quantitative susceptibility mapping*, SIAM J. Imaging Sci., 9 (2016), pp. 481–489, https://doi.org/10.1137/15M1039742.
[43] X. Pan, E. Y. Sidky, and M. Vannier, *Why do commercial CT scanners still employ traditional, filtered back-projection for image reconstruction?*, Inverse Problems, 25 (2009), 123009.
[44] H. S. Park, J. K. Choi, and J. K. Seo, *Characterization of metal artifacts in x-ray computed tomography*, Comm. Pure Appl. Math., 70 (2017), pp. 2191–2217.
[45] B. Petersen, *Introduction to the Fourier Transform and Pseudo-Differential Operators*, Pitman, Boston, MA, 1983.
[46] E. T. Quinto, *The dependence of the generalized Radon transform on defining measures*, Trans. Amer. Math. Soc., 257 (1980), pp. 331–346.
[47] E. T. Quinto, *Singularities of the X-ray transform and limited data tomography in* $\mathbb{R}^2$ *and* $\mathbb{R}^3$, SIAM J. Math. Anal., 24 (1993), pp. 1215–1225, https://doi.org/10.1137/0524069.
[48] E. T. Quinto, *Exterior and limited angle tomography in non-destructive evaluation*, Inverse Problems, 14 (1998), pp. 339–353.
[49] E. T. Quinto, *An introduction to x-ray tomography and radon transforms*, in The Radon Transform and Applications to Inverse Problems, G. Ólafsson and E. T. Quinto, eds., Proc. Sympos. Appl. Math. 63, AMS, Providence, RI, 2006, pp. 1–23.
[50] E. T. Quinto, *Support Theorems for the Spherical Radon Transform on Manifolds*, Int. Math. Res. Not., 2006 (2006), 67205.
[51] A. G. Ramm and A. I. Zaslavsky, *Singularities of the Radon transform*, Bull. Amer. Math. Soc. (N.S.), 28 (1993), pp. 109–115.
[52] G. Rigaud, *On analytical solutions to beam-hardening*, Sens. Imaging, 18 (2017), 5.
[53] W. Rudin, *Functional Analysis*, McGraw–Hill, New York, 1973.
[54] L. Shen, E. T. Quinto, S. Wang, and M. Jiang, *Simultaneous reconstruction and segmentation with the Mumford-Shah functional for electron tomography*, in Proceedings of the 38th Annual International Conference of the IEEE Engineering in Medicine and Biology Society (EMBC), 2016, pp. 5909–5912.
[55] P. Stefanov and G. Uhlmann, *Is a curved flight path in SAR better than a straight one?*, SIAM J. Appl. Math., 73 (2013), pp. 1596–1612, https://doi.org/10.1137/120882639.
[56] F. Trèves, *Introduction to Pseudodifferential and Fourier Integral Operators*, *Volume* 2: *Fourier Integral Operators*, Plenum Press, New York, London, 1980.
[57] J. Vogelgesang and C. Schorr, *Iterative region-of-interest reconstruction from limited data using prior information*, Sens. Imaging, 18 (2017), 16.
[58] F. W. Warner, *Foundations of Differentiable Manifolds and Lie Groups*, Grad. Texts in Math. 94, Springer-Verlag, New York, Berlin, 1983.
[59] Y. Yang, S. S. Hakim, S. Bruns, K. N. Dalby, K. Uesugi, S. L. S. Stipp, and H. O. Sørensen, *Effect of cumulative surface on pore development in chalk*, submitted.